

Geometry-Driven Detection, Tracking and Visual Analysis of Viscous and Gravitational Fingers

Jiayi Xu, Soumya Dutta, Wenbin He, Joachim Moortgat, and Han-Wei Shen

Abstract—Viscous and gravitational flow instabilities cause a displacement front to break up into finger-like fluids. The detection and evolutionary analysis of these fingering instabilities are critical in multiple scientific disciplines such as fluid mechanics and hydrogeology. However, previous detection methods of the viscous and gravitational fingers are based on density thresholding, which is susceptible to the user-specified threshold value. Also, the geometric structures of fingers and their evolution are little studied. In this work, we explore the geometric detection and evolution of the fingers in detail to elucidate the dynamics of the instability. Guided by a new ridge voxel detection method, we first extract finger cores from three-dimensional (3D) scalar fields. After skeletonizing finger cores into skeletons, we design a spanning tree based approach to capture how fingers branch in 3D space from the finger skeletons. Finally, we devise a novel geometric-glyph augmented tracking graph to study how the fingers and their branches grow, merge, and split over time. Feedback from earth scientists demonstrates the usefulness of our approach to analyzing the evolution of fingers.

Index Terms—Viscous and gravitational fingering, topological and geometric data analysis, ridge voxel detection, tracking graph.

1 INTRODUCTION

IN the context of fluid flow in subsurface porous media (e.g., rock formations), *fingering* refers to flow instabilities when either an invading fluid has a much lower viscosity than the displaced fluid (i.e., viscous fingering), or when a denser fluid flows on top of a lighter fluid (i.e., gravitational fingering). Fingering instabilities lead to a highly non-linear and complex evolution of the displacement front between different fluids [1], [2]. Understanding and predicting flow instabilities is critical in a variety of scientific fields including fluid mechanics [3], [4], computational fluid dynamics (CFD) [5], and hydrogeology [1], [6]. Fingering is generally detrimental when the objective is to displace a viscous fluid (e.g., oil recovery through waterflooding) but can be beneficial when the aim is to mix two fluids, for instance, in the sequestration of carbon dioxide (CO₂) [7], [8] in deep water-saturated formations.

In this work, we focus on the latter application, in which gravitational fingering helps to mix dissolved CO₂ throughout the aquifer. This, in turn, helps to guarantee the storage permanence of CO₂ [2], [9]. We illustrate the challenges and high-level motivations for detection and visualization of the fingering process from two perspectives: (1) domain-specific requirements obtained from an expert, and (2) limitations of

previous evolutionary analyses for viscous and gravitational fingers. Below we expand on each of these.

We involved an expert in Earth Sciences to help us comprehend the challenges and domain-specific requirements of this work. Uniquely identifying fingers is challenging because fingers are unstable structures in the fluids, and result from complex fluid interactions. However, flow instabilities, whether in the subsurface or space, have recently been found to obey specific universal scaling laws (e.g., [2], [9]). Such scaling laws can be used to estimate the severity and evolution of flow instabilities for different sets of conditions, without having to redo high-resolution and thus computationally expensive simulations. To reveal those scaling laws, the analysis of pattern formations is critical, i.e., the onset, growth, merging, and splitting of fingers and the connectivity between fingers in space and time. The earth scientist pointed out that tracking and quantifying these features in a 3D volume, to the best of his knowledge, is not possible with any standard visualization tools.

Extracting fingers is challenging, and different detection techniques have been proposed [5], [6], [10], [11], [12], [13]. However, the existing detection techniques use a density or concentration threshold to filter the data first, which is sensitive to the used threshold value. For example, a high threshold may lead to the loss of low-density fingertips, and a low threshold may result that different fingers are not separated. Also, previous detection methods regard each finger as a single entity without further analyzing its internal geometric structures.

In this study, we propose a geometry-driven solution to satisfy the requirements of scientists and analyze geometric structures of fingers. Guided by a ridge voxel detection method, we first extract finger cores, the central regions of fingers, from the data of 3D density fields. Based on the extracted finger cores, we obtain the complete volume of fingers, and produce finger skeletons to acquire overall geometric features of fingers in space. We then propose a span-

- J. Xu is with the Department of Computer Science and Engineering, The Ohio State University, Columbus, OH, 43210.
E-mail: xu.2205@osu.edu
- S. Dutta is with the Science at Scale Team, Los Alamos National Laboratory, Los Alamos, NM 87545.
E-mail: sdutta@lanl.gov
- W. He is with the Department of Computer Science and Engineering, The Ohio State University, Columbus, OH, 43210.
E-mail: he.495@osu.edu
- J. Moortgat is with the School of Earth Sciences, The Ohio State University, Columbus, OH, 43210.
E-mail: moortgat.1@osu.edu
- H.-W. Shen is with the Department of Computer Science and Engineering, The Ohio State University, Columbus, OH, 43210.
E-mail: shen.94@osu.edu

Manuscript received February 26, 2019; revised September 27, 2019.

ning tree based algorithm to construct finger branches from finger skeletons. We visualize fingers and their branches as geometric glyphs, and nest the glyphs into a tracking graph so that we can track and compare fingers and branches efficiently. Hence, our contributions are twofold:

- 1) We propose a new ridge voxel detection technique based on Taylor’s theorem, which is inspired by the detection of pixels having ridge points in [14], to guide the extraction of finger cores from 3D scalar density fields. Furthermore, we provide a spanning tree based heuristic algorithm for the construction of finger branches from finger skeletons.
- 2) We offer an interactive visual analytics system that allows efficient exploration of fingers over space and time with minimized occlusion. Our system incorporates a novel geometric-glyph augmented tracking graph that reveals the temporal evolution of the fingers and their branches effectively.

2 APPLICATION BACKGROUND

In this section, we elaborate on the concepts for the formation of fingers, discuss the domain-specific requirements, and summarize the limitations of previous detection and visualizations of viscous and gravitational fingers.

2.1 Viscous and Gravitational Fingers

Viscous and gravitational flow instabilities in porous media result in finger-like features. The *fingering* phenomenon refers to the formation and evolution of such fingers. The fingering instabilities are triggered by adverse mobility or density ratios between displacing and displaced fluids [1]. *Viscous fingering* is caused by viscosity contrasts between fluids: when a less viscous fluid is injected into a more viscous medium, the less viscous fluid tends to penetrate through the more viscous fluid to form elongated finger-like structures [3]. *Gravitational fingering* is caused by contrasts in density between fluids: when a denser fluid resides on top of a less dense fluid, the interface may become unstable. The denser fluid vertically penetrates the lighter fluid to form fingers, while the lighter fluid rises buoyantly.

Data description. The fingering datasets used by this paper were generated from simulations of injecting carbon dioxide (CO₂) from the top of a water-saturated reservoir. The gravitational fingering helps to mix injected CO₂ throughout the aquifer. When CO₂ dissolves in water, it locally increases the water density in the top, which is prone to gravitational instabilities. The CO₂-water front becomes unstable and leads to fingering of CO₂-enriched, denser, water downwards with the upwelling of fresh lighter water. Each simulation data has more than one hundred timesteps. The space for the data is defined within a cuboid reservoir, which has a 30 meters \times 30 meters base and is 40 meters in height. The reservoir is represented by a 3D rectilinear grid (90 \times 90 \times 100) with uneven spacing, where each grid cell is associated with a CO₂ density value.

2.2 Requirements of a Earth Scientist

We discuss the application-specific requirements that were identified by a domain expert who specializes in Earth

Sciences. This earth scientist has ten years of experience in researching fluid injection processes and associated viscous and gravitational fingering instabilities. In his day to day studies, the expert often visually analyzes the fingers using visualization tools such as ParaView [15], VisIt [16], and Tecplot [17]. During our interactions, the scientist mentioned that he was interested in how to visualize the 4D (3D in space plus time) simulations of fluid injection. He stated that, without the ability to look at the data in many different ways effectively, it was often hard to even know what questions to ask or answer. The expert also informed us that the current visualization techniques that he used were not ideal. For example, some domain tools visualize fingers as hollow sheets rather than dense columns; also, the three-dimensional fingers which were visualized by standard visualization methods such as volume rendering and isosurfaces suffered from the occlusion problem. Thus, the expert usually had to cut multiple cross-sections of those fingers to analyze the formation and internal structures of fingers rigorously. However, tracking and quantifying the 3D geometry of these ramified structures in both space and time is virtually impossible with those methods, i.e., how hundreds of distributed fingers grow vertically, spread horizontally, shield and merge at certain timesteps, and then predominantly split into new smaller fingers at other timesteps. Visualizing and quantifying these geometric features provide insights into the analyses of bimolecular reaction [18] and physical flow regimes of, e.g., enhanced or suppressed mixing rates [4], [8]. Moreover, the geometrical features, including widths [7] and tip locations [7] of fingers, have been used to analyze scaling behaviors. However, the vast majority of studies [7], [18] on earth sciences for geometric analysis of fingers are in 2D and often that has been done essentially by hand and visual inspection. He thought that interactive space-time diagrams of the fingers, which can effectively present the finger-specific events such as merging, splitting, and branching of fingers, would be extremely valuable.

2.3 Limitations of Existing Works for Fingers

In this section, we review the methods used previously to detect and visualize viscous and gravitational fingers, and highlight the limitations of the existing methods.

2.3.1 Limitations of Current Detection Methods for Fingers

To detect fingers and their branches, domain scientists require a robust detection method. Since the formation of fingers is extremely non-linear, accurate detection of the fingers is a non-trivial task. To extract fingers from the density (or concentration) scalar fields, previous researchers typically used thresholding on the density value to extract high-density regions, and interpreted the connected (or, close) high-density regions as fingers. In the previous study, Skauge et al. [6] and Fu et al. [10] modeled fingers as high-density vertical lines, which were detected by a peak detection method. However, fingers may have complex branching structures rather than simple vertical lines. Aldrich et al. [11] and Lukasczyk et al. [13] considered each finger to be a connected component of high-density 3D regions and detected fingers through the identification of connected

components. An alternative approach proposed by Favelier et al. [12], instead of detecting the fingers directly, detected the fingertips first and segmented the 3D volume by a watershed traversal method to obtain the full fingers from the fingertips. Luciani et al. [5] studied particle data of fingering, and grouped particles with close locations and concentrations to be fingers.

These existing methods [5], [11], [12], [13] usually require a specific density or concentration threshold to filter the data first. Even though the previous methods obtained good results, the use of such hard thresholding can make the finger extraction sensitive to the threshold value used. For example, fingertips usually have much lower densities than the finger roots (i.e., top parts of the fingers). If the threshold is too large, these fingertips that do not satisfy such threshold may be missed. If the threshold is too small, different fingers cannot be segmented because regions between fingers also have densities such as Fig. 6b. Lukasczyk et al. [19] also reported that it is not sufficient to segment fingers based on a certain density threshold.

Furthermore, the previous methods [5], [11], [12], [13] typically concentrate on detecting each finger as a single entity, but our application requires more detailed geometric structures of fingers (e.g., the branching of fingers), which are essential to the scientists in understanding flow instabilities [20], [21], [22], [23].

2.3.2 Limitations of Current Tracking Graphs for Fingers

When it comes to the visualization of time-varying fingers, none of the existing tracking visualizations focus on the geometric evolution of the fingers. The tracking graphs provided by Aldrich et al. [11] display fingers at each timestep as points in a column. Aldrich et al. [11] used hues to encode different fingers and linked related fingers between adjacent timesteps by curves. In recent work, Lukasczyk et al. [19] proposed nested tracking graphs, which can depict the evolution of level-sets of density fields and visualize the evolution of fingers across multiple specified density thresholds. The lack of tracking graphs for the geometric evolution of fingers that encodes the branching information and is not sensitive to the specified density thresholds further motivates us to develop a new geometry-driven tracking graph for the analysis of the fingering process.

3 RELATED WORK

We discuss related techniques to our geometry-driven approach in the following.

Ridge detection methods. Ridges originally are structures of surface topography whose mathematical properties were studied by de Saint-Venant [24]. In mathematics, the ridges of a smooth function are a set of curves or surfaces whose points are local maxima of the function in a certain number of dimensions; specifically, ridge lines are curves whose points are local maxima in $n - 1$ dimensions if the dimensionality of the whole space is n . The concept of ridges has been used to detect and extract curvilinear structures in computer vision [14], [25] and scientific visualization [26], [27]. In computer vision, we regard the grey-level image as a 2D scalar field, and extract curvilinear structures such as roads [14] and human fingers [25] by applying the ridge

line detection method. In scientific visualization, definitions of ridges are extended to volumetric data [26], [27].

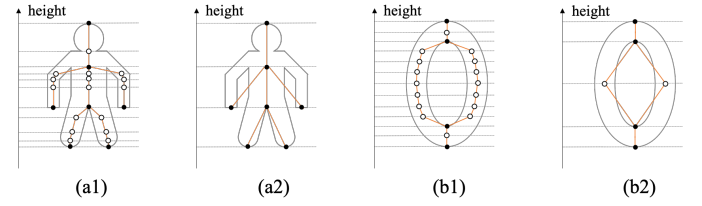


Fig. 1: We explain how to extract the skeleton of a 2D human-like object and an O-shaped object by the Reeb-graph-based method. We first shrink the level-sets of the height function to get intermediate results for the two objects in (a1) and (b1). Solid circles represent critical points of the height function; hollow circles represent passing points. Next, we remove the intermediate passing points, and connect the critical points with straight lines to simplify the intermediate skeletons to obtain the Reeb graph embeddings in (a2) and (b2). Note that the O-shaped object contains a loop, so we preserve two passing points in (b2) to display the cycle structure visually.

Reeb graph skeletonization. The Reeb graph based skeletonization is one of the standard skeleton-extraction approaches [28]. The Reeb graph obtains the topology of a compact manifold by following the evolution of the level-sets of the height function defined on the manifold. Nodes in the Reeb graph represent critical points of the height function, and edges correspond to connections between critical points [28], [29]. The resulting Reeb graph is not a skeleton; however, Lazarus and Verroust [30] embedded the resulting Reeb graph into the space to get the skeleton of the original object. Fig. 1 is an example to derive skeletons of 2D objects based on Reeb graphs. If an object has no holes inside, the contour tree [31], as a special instance of the Reeb graph, is sufficient for the skeletonization of this object. Topology Toolkit (TTK) [32] offers examples for the shape skeletonization by using the contour tree, and recently supports the Reeb graph based method [33].

4 APPROACH OVERVIEW

In this work, we focus on the detection of geometric structures of fingers and the visualizations of the time-varying fingers with minimized occlusion. Fig. 2, a schematic diagram, presents an overview of our solution. From the raw density fields, we apply a ridge voxel guided detection method to extract central structures of fingers as finger cores. We expand the finger cores to obtain the complete volume of fingers, and display the volume of fingers in the spatial domain by using the volume rendering. We skeletonize the finger cores into finger skeletons by using a Reeb graph based skeletonization, and draw the finger skeletons in 3D space to provide the overall geometric structures of fingers. Also, we project finger skeletons onto a plane to observe spatially relative positions between fingers. We construct finger branches from the finger skeletons using a variant of spanning tree method. Given the branches of fingers, we adopt various tree-based visualization methods

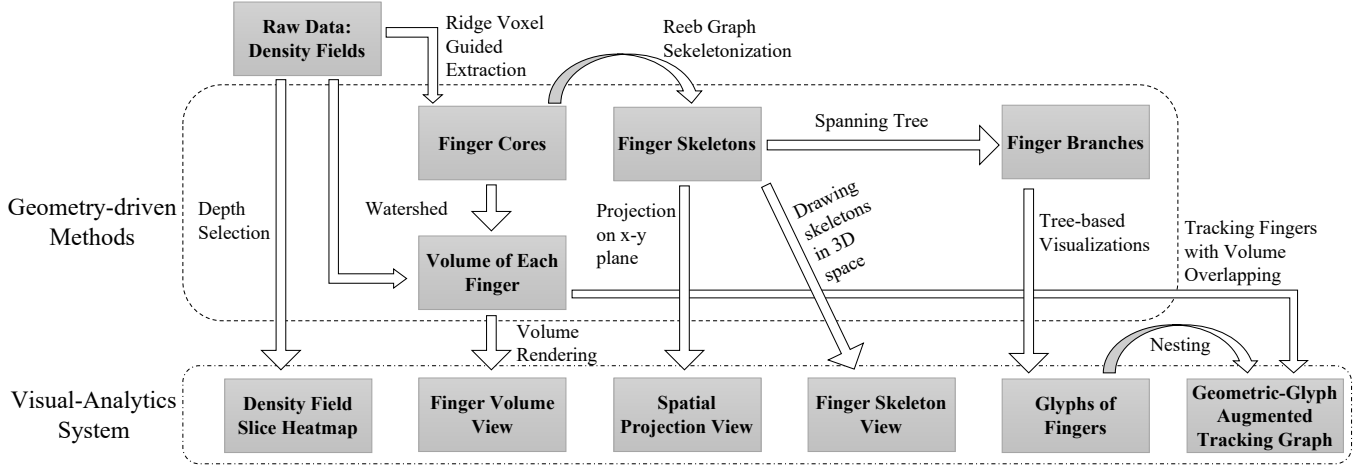


Fig. 2: We present a schematic diagram of our geometry-driven approaches for viscous and gravitational fingering.

to represent different aspects of finger branches. Finally, we develop a geometric-glyph augmented tracking graph to study how the fingers evolve geometrically. Also, on the tracking graph, we link temporally related fingers, and design interactions to identify the change of branches over time.

5 GEOMETRY-DRIVEN DETECTION OF VISCOUS AND GRAVITATIONAL FINGERING

In this section, we present the geometry-driven detection technique for the viscous and gravitational fingering process in detail. Since the fingering process is complex and non-linear, precise descriptors for robustly extracting the fingers are unavailable in the earth science domain. So, in order to develop a reliable technique for extracting fingers, we model the central regions of the fingers as ridges. In our work, the finger cores include both the ridge regions as well as a portion of nearby volume to robustly capture the connections among neighboring finger branches. The final extracted fingers consist of the finger cores and the connected lower-density regions covering the finger cores. Note that, in contrast to previous methods that extract fingers based on density thresholding, our approach first extracts the core structures of fingers guided by a ridge voxel detection method, then, expand the finger cores to the complete volume of fingers. As a result, our approach is not sensitive to a hard density threshold value, and so, low-density fingertips and branches can be preserved. We skeletonize finger cores into linear geometric structures, and construct finger branches from finger skeletons by a spanning tree based approach; we also trim finger skeletons to emphasize persistent branches. Finally, the temporal relationships among fingers at consecutive timesteps are realized based on volume overlapping.

5.1 Ridge Voxel Guided Extraction of Finger Cores

The extraction of finger cores is guided by a ridge voxel detection method. According to our domain scientist, one of the causes of fingering is the diffusive process. The diffusion of CO_2 is driven by compositional gradients (i.e.,

the difference of CO_2 /water composition). Through the diffusive process, CO_2 volume tends to spread out from high-density regions to low-density regions; the regions with higher densities usually form the center of finger structures. Note that the *ridge voxels*, where voxels (i.e., grid cells at a timestep) contain ridge points, are regions with locally higher densities in density fields. Therefore, the finger cores are extracted guided by the ridge voxel detection technique.

To obtain regions with locally higher densities, we filter the 3D domain to identify ridge voxels. However, conventional ridge line detection methods [26], [27] may not be suitable to extract finger cores for two reasons.

- 1) Traditional methods detect precise paths of ridge lines across voxels. However, according to the study of Damon [34], exact ridge lines do not represent branching structures well, which may lead to disconnected finger branches. In contrast, our proposed method detects ridge voxels instead of precise paths of ridge lines, which preserves the necessary branching structures of fingers through preserving the voxels that are close to the ridge lines.
- 2) If multiple ridge lines pass through the same voxels, traditional methods separate the distinct ridge line pieces in the shared voxels, which is not desirable in our application. When the CO_2 volumes containing these ridge line pieces overlap at the shared voxels, these CO_2 volumes interact with each other at the shared voxels; the interactions between CO_2 volumes usually correspond to the branching of fingers. Hence, unlike the traditional methods where ridge lines across shared voxels are considered separate, we group voxels that contain such ridge lines into the same finger structure.

In the 3D space, we use Taylor's theorem to detect ridge voxels, which is inspired by Steger's 2D detection method [14]. When extracting 2D curvilinear structures, Steger [14] used Taylor's theorem to locally approximate the grey-level function centered at each pixel of 2D image to detect pixels having ridge points. Note that, although the whole ridge structure is complex, ridge points are local features, namely, are the features that satisfy the local criterion [25], [35]. So, the locally approximated function and derivatives are sufficient to detect the points on ridge lines [14], [26], [27].

In the following, we discuss details of our ridge voxel detection method, which determines whether a given voxel contains ridge points of a 3D density field based on Taylor's theorem.

Let the center point of the given voxel be noted as $\mathbf{p}_0 = (x_0, y_0, z_0)^T$. Let r_x , r_y , and r_z be the first-order partial derivatives at the midpoint \mathbf{p}_0 . Then, the Jacobian matrix, which consists of the first-order partial derivatives, at the center point is defined by

$$J(\mathbf{p}_0) = J(x_0, y_0, z_0) = (r_x, r_y, r_z)^T. \quad (1)$$

The Hessian matrix, consisting of the second-order partial derivatives, at the center point is given by

$$H(\mathbf{p}_0) = H(x_0, y_0, z_0) = \begin{bmatrix} r_{xx} & r_{xy} & r_{xz} \\ r_{yx} & r_{yy} & r_{yz} \\ r_{zx} & r_{zy} & r_{zz} \end{bmatrix} \quad (2)$$

In our work, we estimate the derivatives of the Jacobian matrix and the Hessian matrix locally, which is detailed in App. A.

We use the second-order multivariate Taylor polynomial to approximate the density function locally based on the estimated derivatives at the center point. Let $\mathbf{p} = (x, y, z)^T$ be any point within the voxel. Let $f(\mathbf{p})$ be the locally approximated density function within the voxel, which is defined by

$$f(\mathbf{p}) = f(\mathbf{p}_0) + J(\mathbf{p}_0)^T \Delta \mathbf{p} + \frac{1}{2} \Delta \mathbf{p}^T H(\mathbf{p}_0) \cdot \Delta \mathbf{p} \quad (3)$$

where $\Delta \mathbf{p}$ is the displacement of \mathbf{p} to the midpoint \mathbf{p}_0 . In other words, $\Delta \mathbf{p} = \mathbf{p} - \mathbf{p}_0$. Hence, the Jacobian matrix of $f(\mathbf{p})$ is

$$J(\mathbf{p}) = (f_x(\mathbf{p}), f_y(\mathbf{p}), f_z(\mathbf{p}))^T = J(\mathbf{p}_0) + H(\mathbf{p}_0) \cdot \Delta \mathbf{p} \quad (4)$$

According to Equation 3, the Hessian matrix of $f(\mathbf{p})$ is uniform within the voxel, namely,

$$H(\mathbf{p}) = H(\mathbf{p}_0) \quad (5)$$

To examine whether there exists ridge points within the voxel, we refer to the criterion of ridge points [25]. Note that, in the 3D space, the size of the Hessian matrix $H(\mathbf{p})$ is 3×3 ; hence, the Hessian matrix has three eigenvectors with three corresponding eigenvalues. We sort all the three eigenvectors by the absolute values of their eigenvalues in descending order. Let the two eigenvectors, whose absolute eigenvalues are top two maximal, be $\vec{v}_1 = (v_{1x}, v_{1y}, v_{1z})^T$ and $\vec{v}_2 = (v_{2x}, v_{2y}, v_{2z})^T$. Then, the first-order directional derivatives at the point \mathbf{p} along the two eigenvectors, \vec{v}_1 and \vec{v}_2 , are

$$d_i(\mathbf{p}) = \vec{v}_i^T J(\mathbf{p}), \quad i = 1, 2. \quad (6)$$

According to Lindeberg's criterion [25], this point is a ridge point if and only if the two conditions are satisfied:

Condition One: The two second-order directional derivatives at the point \mathbf{p} along the two eigenvectors, \vec{v}_1 and \vec{v}_2 , are both smaller than zero.

Condition Two: The two first-order directional derivatives (Equation 6) are both zeros.

Given a 2D image, to detect the ridge point within a pixel conveniently, in addition to the basic ridge criterion [25],

[35], Steger's method [14] has one additional assumption: the ridge point should lie on the line which passes the center of a pixel and is at the direction of the eigenvector with the maximal absolute eigenvalue. However, this assumption brings more restriction to the detection of ridge points within voxels in the 3D space and may lead to missing ridge voxels. Hence, our approach derives the inequalities solely from the basic ridge criterion [25], [35] to determine whether a voxel contains ridge points or not, which is illustrated below.

We examine whether there exists a ridge point $\mathbf{p}_1 = (x_1, y_1, z_1)^T$ within the given voxel based on Condition One and Two of Lindeberg's criterion [25].

To satisfy Condition One, we get second-order directional derivatives at \mathbf{p}_1 along the two eigenvectors, \vec{v}_1 and \vec{v}_2 , of the Hessian matrix $H(\mathbf{p}_1)$ to ensure that the second-order directional derivatives are less than zero. A fact is that the eigenvalues of a Hessian matrix are the second-order directional derivatives along the corresponding eigenvectors exactly. Hence, in other words, we examine whether the corresponding eigenvalues of the two eigenvectors, \vec{v}_1 and \vec{v}_2 , are less than zero or not for Condition One. Because $H(\mathbf{p}_1)$ is equal to $H(\mathbf{p}_0)$ through Equation 5, we guarantee that the corresponding eigenvalues of the two eigenvectors \vec{v}_1 and \vec{v}_2 of $H(\mathbf{p}_0)$ are less than zero to satisfy Condition One.

To satisfy Condition Two, we obtain the two first-order directional derivatives at the point \mathbf{p}_1 by $d_1(\mathbf{p}_1)$ and $d_2(\mathbf{p}_1)$ of Equation 6, and equate the two derivatives to zeros. Note that we have two equations (i.e., $d_1(\mathbf{p}_1) = 0$ and $d_2(\mathbf{p}_1) = 0$) and three unknowns (i.e., x_1 , y_1 , and z_1) hence we can get expressions of two of the unknowns by polynomials of the third unknown. Without loss of generality, we represent x_1 and y_1 by polynomials of z_1 . Next, we constrain that the point $\mathbf{p}_1(x_1, y_1, z_1)$ is within or on boundary of the voxel to obtain inequities of x_1 , y_1 , and z_1 . We substitute x_1 and y_1 by the polynomials of z_1 to get three inequities only associated with z_1 . If the union of the three inequities of z_1 is not empty, there exists a feasible value of z_1 that satisfies all of the three inequities and exists a ridge point \mathbf{p}_1 within or on the boundary of the voxel that satisfies Condition Two.

Finally, if there exists a feature point \mathbf{p}_1 that satisfies both Condition One and Two, we declare this voxel to be a ridge voxel.

In practice, in addition to ridge voxels, we also include more voxels, that have ridges nearby, into the finger cores to obtain more connections between branches by controlling a spacing parameter. The sensitivity of the method depends on the spacing parameter, and the details about it can be found in App. B. The produced results are demonstrated in Fig. 3 and Fig. 4.

Observed from Fig. 3b, almost all finger cores are connected through the high-density hexagonal cells in the top layer; the *top layer* is the diffusive boundary layer contained in the top grid cells. Hence, when separating vertical finger cores, we ignore the part of finger cores in the top layer, as suggested by the previous works [5], [11], [13]. Then, we define each *individual finger core* as a connected component of the finger core voxels, excluding the top layer.

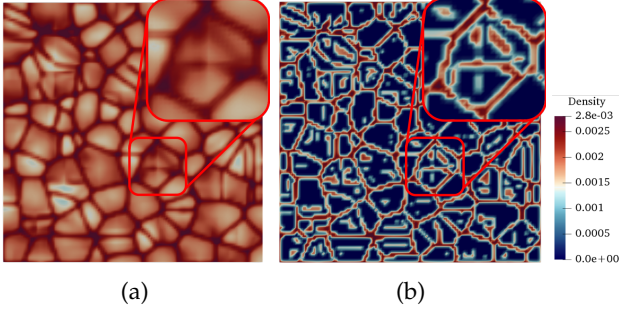


Fig. 3: We show the top view of (a) the raw 3D space and (b) the extracted finger cores. As the same places are highlighted in (a) and (b) by red, the ridge-guided method detects high-density hexagonal cells in the top grid cells and high-density curvilinear structures inside the hexagonal cells.

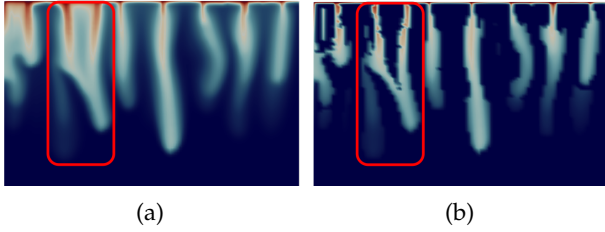


Fig. 4: We show the side view of (a) the raw 3D domain and (b) the extracted finger cores. As the same finger is highlighted in (a) and (b) by red, the ridge-guided method captures the geometric structure of a finger with splitting and fusion of branches.

5.2 Segmentation of Complete Finger Volume in Space

We recover complete fingers by segmenting the 3D density field at each timestep into connected subfields. In computer vision, the watershed technique is well-known for segmenting images. In a previous study, Favelier et al. [12] segmented a scalar field by using the watershed traversal method [36] to capture fingers given separated fingertips. Following a similar strategy, given separated individual finger cores, we use a flood-filling watershed algorithm to extract the full fingers from the 3D domain. In the following, we list steps to perform the segmentation.

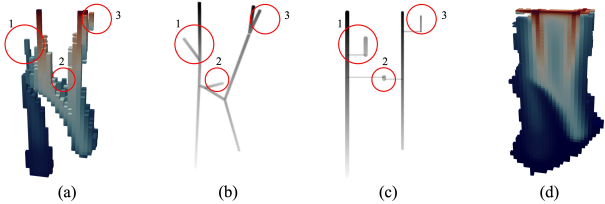


Fig. 5: We display the results of our methods for a simple finger. We show four images: (a) the finger core, (b) the finger skeleton, (c) the linear glyph of the finger, and (d) the complete finger volume. Three small branches are circled by red and labeled with numbers for readers to identify the correspondence efficiently.

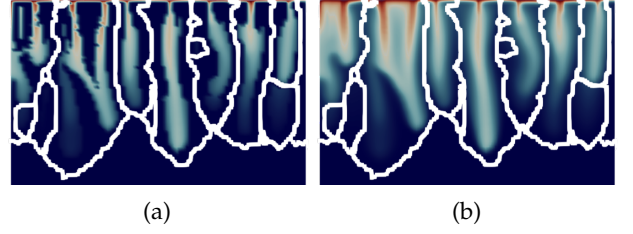


Fig. 6: We show the segmentation boundaries by using white lines on (a) the finger cores and (b) the raw 3D domain.

Step 1 We assign a unique index to each individual finger core; all voxels of each individual finger core are labeled using the index of the finger core. We insert all the labeled voxels into a first-in-first-out (FIFO) queue.

Step 2 We get a labeled voxel from the queue, and propagate its label to its unlabeled adjacent voxels; note that, only the voxels with non-zero densities are considered for labeling. These newly labeled voxels are then inserted into the queue. The second step is repeated until the queue is empty.

We display boundaries between segmented fingers in Fig. 6 by white lines. As a result, the shared low-density regions between finger cores are separated evenly and are assigned to the contiguous finger cores by our method. Fig. 5d presents the extracted voxels of a finger; more complex fingers are displayed in (b) and (c) of both Fig. 7 and Fig. 8. The segmented fingers satisfy the cognition of the earth scientist regarding individual fingers.

5.3 Construction of Geometric Structures of Fingers

In this section, we construct geometric structures of fingers. We first obtain finger skeletons from finger cores. Finger branches are extracted from finger skeletons afterwards. We further trim finger skeletons by removing short branches and cycles.

5.3.1 Reeb Graph Based Skeletonization

We use the Reeb graph based method [13], [28], [29], [30], [33] to obtain finger skeletons. Fingers have two important topological and geometric characteristics: the branching and the height. The branching is critical to scientists in understanding flow instabilities [20], [21], [22], [23]. Due to the gravity, fingers stretch vertically; based on the height, we estimate the vertical speed of growth of fingers to analyze the stretching process. In computational geometry, Reeb graphs are well-known for their ability to show the skeletons of a 3D object [28] and preserve the branching and the height of a 3D object accurately [29]. Contour tree [31] is an alternative approach for shape skeletonization. However, in our application, voxels that do not belong to finger cores are removed, which may leave holes in the volume of finger cores (e.g., Fig. 8a); in other words, the volume of finger cores may have torus-like structures. Hence, the contour tree based method is not appropriate for our application. Fig. 1 explains the skeleton extraction from a 2D human-like object and an O-shaped object by using the Reeb graph based method. The intermediate skeletons (e.g., (a1) and (b1) of Fig. 1) contain all the geometric information of the object;

the final results (e.g., (a2) and (b2)) usually only contain critical points of the height function and edges that connect the critical points, which provides simplicity and clearness to visualizing the branching and the height information. If one requires to preserve more geometric information such as the curvature and length of branches, the intermediate skeletons (e.g., (a1) and (b1)) can be directly used.

We skeletonize the extracted individual finger cores based on Reeb graphs. We sweep voxels of finger cores vertically and shrink the connected components to points to form Reeb graphs. The resulting Reeb graphs are then embedded in the 3D space to obtain skeletons of the fingers by preserving the branching and the height information. The resulting skeleton of a simple finger is shown in Fig. 5b. Complex examples are shown in (d) of both Fig. 7 and Fig. 8.

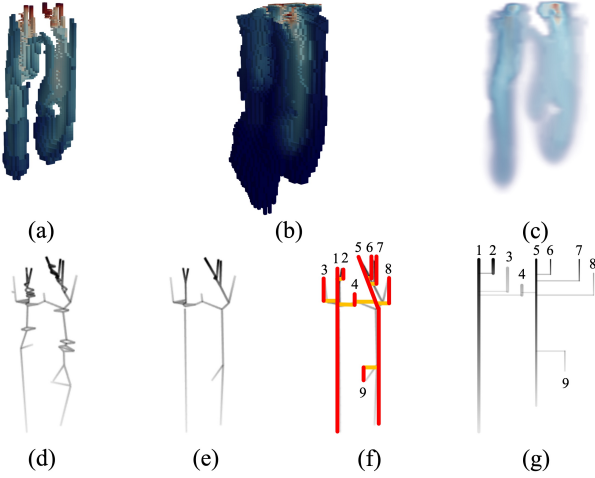


Fig. 7: We display a complex finger with (a) the finger core, (b) the complete finger volume, (c) the volume rendering image of (b), (d) the raw finger skeleton, (e) the trimmed finger skeleton, (f) the constructed branches from (e), and (g) the linear glyph that is based on (f). In (f), the branches are represented by red lines, and the connections between branches are represented by orange lines. In (f) and (g), the same numbers label corresponding branches.

5.3.2 Spanning Tree Based Extraction of Finger Branches

We create finger branches for two reasons. First, our earth scientist is more interested in how fingers ramify from top to bottom rather than all the connections within finger skeletons. Second, finger branches as a tree structure can be visualized with minimized occlusion.

We extract finger branches from finger skeletons by a spanning tree based heuristic algorithm. Due to the stretching process, finger branches grow downward; based on that, branches are assumed to be vertical linear structures in the finger skeletons. Note that finger skeletons in this paper are Reeb graphs that are embedded in 3D space. Existing works [37], [38] suggest extracting spanning trees from the Reeb graph embeddings to create branches. Following the suggestions, the steps of spanning tree based finger branch extraction are as follows:

Step 1 We identify vertical structures from an embedded Reeb graph (i.e., a finger skeleton). From the graph, we

search the longest downward path (i.e., the path with the longest height persistence) to be a new branch by using the breadth-first search; note that on a downward path, the height of a point should be strictly larger than the height of its following point. If multiple paths in this graph are the longest, we use the one with the smallest deviation on the x - y plane. Next, we delete the points and edges of this new branch from the given graph, and repeat Step 1 until the given graph becomes empty. After obtaining all the branches, we insert the longest one into a FIFO queue, and mark this one to be enqueued.

Step 2 We build connections between branches. We obtain a branch from the queue, and identify which unmarked branches have edges connecting with it in the original graph; we then record such connecting edges. If an unmarked branch has multiple edges connecting with the dequeued branch, we select one of these edges whose endpoint on the dequeued branch is the highest. Finally, we insert the newly identified branches into the queue, and mark these branches to be enqueued.

Fig. 7f shows the constructed branches and the connections between the branches. After building finger branches, we visualize constructed branches by tree-based visualizations to minimize occlusion, such as Fig. 5c and Fig. 7g.

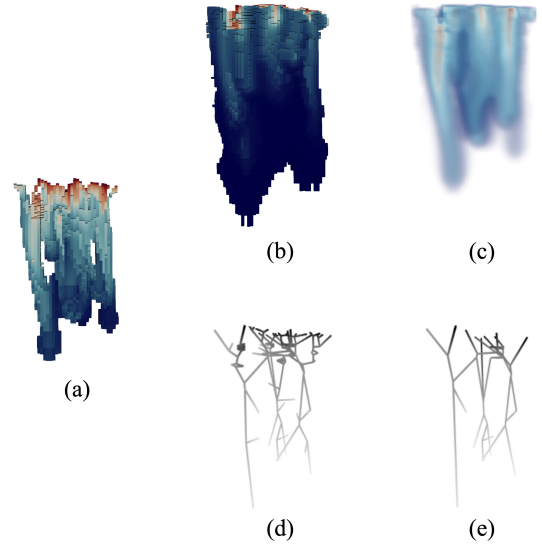


Fig. 8: We display a complex finger including (a) the finger core, (b) the complete finger volume, (c) the volume rendering image of (b), (d) the raw finger skeleton, and (e) the trimmed finger skeleton.

5.3.3 Trim of Finger Skeletons with Removal of Short Branches and Cycles

We trim the Reeb-graph based finger skeletons. When a finger has a complex structure, it is inefficient to acquire essential geometric information from the full skeleton. For example, in Fig. 8d, short branches occlude persistent branches and hinder the perception of the overall geometric structure. Hence, we prune the finger skeletons to preserve the most relevant geometric information of the fingers and minimize the occlusion. The trim of the Reeb-graph based skeletons is

based on the geometric characteristic: the height persistence of fingers and their branches. We define *height persistence of a finger* as the height difference between the fingertip and the finger root. Similarly, *height persistence of a finger branch* is the height difference between the highest point and deepest point on the branch. To trim Reeb graphs, Bauer et al. [39] suggested removing features with persistence smaller than a threshold. Specifically, Carr et al. [40] suggested pruning away small leaves. In addition to short leaves, Doraiswamy and Natarajan [38] also suggested removing short cycles in Reeb graphs. Hence, to prune finger skeletons, we remove short leaf branches (i.e., each of the branches has only one edge to other branches) and certain short loops. To remove these branches with short height persistence, we remove points on these branches and delete connections related to these points from finger skeletons. We remove specific short loops that have short persistence and each of the loops has exact two critical points, such as (b2) of Fig. 1. Certain critical points may become passing points after the removal; we remove these points as well. As a result of the trim, the geometric structure of fingers can be readily understood. The trimmed skeletons are shown in (e) of both Fig. 7 and 8.

A potential concern is that, by only using height persistence, the trim of finger skeletons filters out short but high-density or thick branches. Regarding this concern, our method supports to put weights on the height persistence of branches. The weighted height persistence of branches is equal to their height persistence multiplied by the average densities or thickness of the branches.

5.4 Volume Overlapping Based Tracking of Fingers and Branches

To track fingers and their branches over time, we need to relate fingers and their branches at consecutive timesteps. Mapping correct features, fingers in this case, at successive timesteps is known as the correspondence problem. Silver and Wang [41] proposed a volume overlapping based method for solving this problem on scalar data. Because fingers usually flow downward and do not move entirely with a significant horizontal deviation, recently, researchers have adopted such volume overlapping based method for tracking fingers. Favelier et al. [12] connected each finger at a timestep only to the finger with the largest volume overlapping at the next timestep, and draw corresponding fingers by same colors. Aldrich et al. [11] and Lukaszczuk et al. [13] relate fingers between adjacent timesteps with any volume overlapping, which offers more connections to track the full temporal evolution of fingers and is used in this paper.

To estimate overlapping volume between the fingers at consecutive timesteps, we compute how many grid cells that are shared by the fingers. We link all the fingers at adjacent timesteps who share grid cells. The number of shared cells and densities of these shared cells reflect the strength of connections between linked fingers. Also, the shared cells have positions that reveal where the volume of the fingers overlaps. After identifying the correspondence between fingers, we further relate branches of corresponding fingers also based on the overlapping of grid cells.

6 VISUALIZATION OF VISCOUS AND GRAVITATIONAL FINGERING

We create an interactive visual-analytics system to perform spatio-temporal analyses on the geometric structures of the viscous and gravitational fingers. In our system, we present juxtaposed visualizations so that users can compare fingers over space and time. Fig. 9 shows the complete visual-analytics system, which consists of six panels marked as (a)-(f). (a) the depth selection panel allows users to select a depth of interest in the spatial domain. Then, (b) the density field slice view displays the density field at the selected depth as a 2D heatmap. (c) the spatial projection panel presents a high-level spatial view, and uses convex hulls to indicate the fingers projected on the x - y plane. Users can also observe different facets of fingers in detail through (d) a volume rendering image and (e) a 3D skeleton visualization. Finally, at the bottom of Fig. 9, (f) the geometric-glyph augmented tracking graph displays the evolution of fingers. All the views in our system are interactive and coordinated together to enable coherent visual analyses. In the following, we describe each of these panels in detail.

6.1 Depth Selection and Density Field Slicing

Density field slicing is an important tool for scientists to study the change of densities inside fingers in space. In Fig. 9a, the depth selection panel, our system allows users to drag a depth slider to select a depth of interest; the 3D spatial region below the selected depth is highlighted by gray color in a 3D cube. The density field slice at the selected depth is then extracted and shown as a 2D heatmap in Fig. 9b. The finger volume and skeleton views (Fig. 9de) are updated to show finger structures under the selected depth only. The selected depth is set to the top of the 3D domain initially, because CO₂ is injected from the top of the aquifer.

6.2 Spatial Projection of Fingers

Before showing individual fingers, a high-level spatial view is required to reveal the relative positions between fingers so that scientists can efficiently observe how fingers interact spatially. To enable that, we use the spatial projection of fingers. Convex hull and Voronoi treemap are further applied to display the projected fingers, as detailed below.

Convex hull We project critical points of finger skeletons onto the x - y plane. We then draw a convex hull to enclose the projection of the critical points of each finger. The convex hull representation, such as Fig. 9c, demonstrates the coverage of each finger in space, and help scientists identify large fingers instantly. This view also supports the selection of a finger of interest to display the volume and skeleton of the selected finger. The convex hull of a selected finger is also superimposed on the density field slice view, as shown in Fig. 9b to confirm the existence of the selected finger in the density field. In addition, we project centroid points of finger skeletons onto the x - y plane for both the density field slice and spatial projection view.

Voronoi treemap To reveal information of finger branches, we use the Voronoi treemap technique [42] to represent finger branches by Voronoi cells, and embed the resulting Voronoi cells in the convex hulls of fingers instead

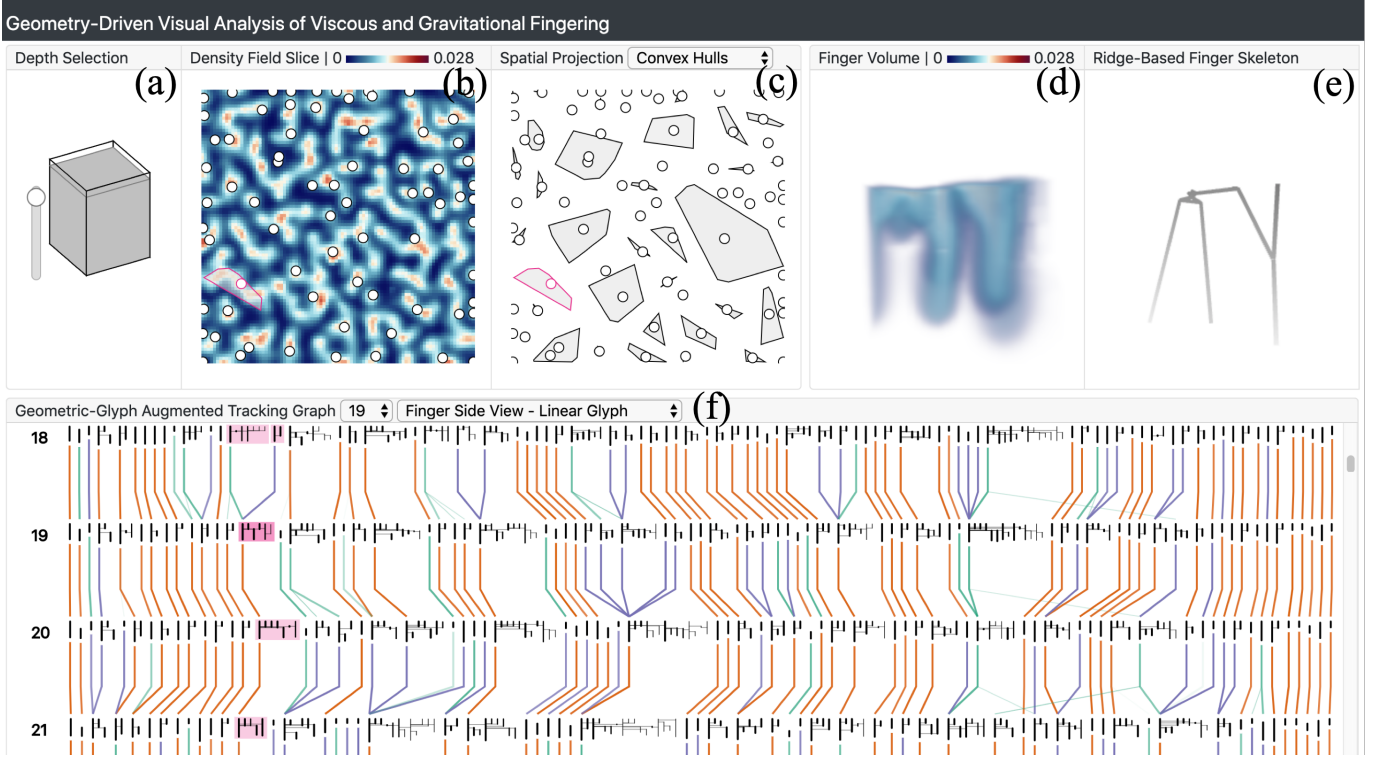


Fig. 9: A geometry-driven visual-analytics system is used to study viscous and gravitational flow instabilities. (a) Depth slider is used to specify a depth of interest. The 3D domain under the specified depth is shown for analysis. (b) View of a density slice at the specified depth, which also shows centroid points of fingers projected onto the x - y plane. (c) The spatial projection view displays the fingers projected onto the x - y plane using scattered convex hulls. (d) The finger volume view displays the density field of a selected finger. (e) The finger skeleton view shows the geometric structure of a selected finger in 3D space. (f) Geometric-glyph augmented tracking graph visualizes the geometric evolution of fingers based on geometry-driven planar glyphs.

of centroid points such as Fig. 10f. Users can select to observe either centroid points for simplicity or Voronoi cells for details of finger branches. Dark Voronoi cells mean that the corresponding finger branches exist in the deep region of the 3D domain. More precisely, the darkness of Voronoi cells encodes the average depth of critical points that are in the corresponding finger branches. The size of a Voronoi cell encodes the topological complexity of the corresponding finger branch. Intuitively, a finger branch having more critical points usually indicates that this finger branch is connected to more other branches and thus is more complex in terms of its topological structure. Hence, we define *topological complexity of a finger branch* by the number of critical points on the branch skeleton. Moreover, if scientists need to under-emphasize low-density or thin branches, the average densities or thickness values of branches are used as weights of critical points for calculating the topological complexity.

6.3 3D Spatial Visualizations of a Selected Finger

We provide 3D volume and skeleton based visualizations for further analyses after selecting a finger of interest. Users can interactively rotate both of the volume and the skeleton to study the 3D structure of the finger from different view-points, and zoom into the representations to study details of the finger structure.

6.3.1 Volume Visualization

The volume rendering image of an individual finger, e.g., Fig. 10ae, visualizes how the density field of the finger appears in the physical domain, which allows scientists to interpret the finger intuitively. Moreover, the ray casting based volume rendering remedies the occlusion on the direct display of voxels (e.g., Fig. 8b) with transparency.

6.3.2 Geometric Skeleton Visualization

To visualize the overall geometric structures of fingers in 3D space, we display the finger skeletons on the screen using orthogonal projection such as Fig. 10b. To recover the density information of fingers, we use intensity gradients along lines to indicate changes in the density of finger branches; hence, high-density branches are highlighted, and low-density branches are under-emphasized.

6.4 Geometric-Glyph Augmented Tracking Graph

The geometric-glyph augmented tracking graphs, as shown in Fig. 9f and Fig. 11, visualize the time-varying fingers. The tracking graphs help scientists identify various evolutionary events of fingers, and analyze how the evolutionary events happen in detail through interactions. Each row of the tracking graph displays the extracted fingers at one timestep; the timestamp is labeled at the left of the panel. Widths of finger glyphs of each row are adjusted according to the

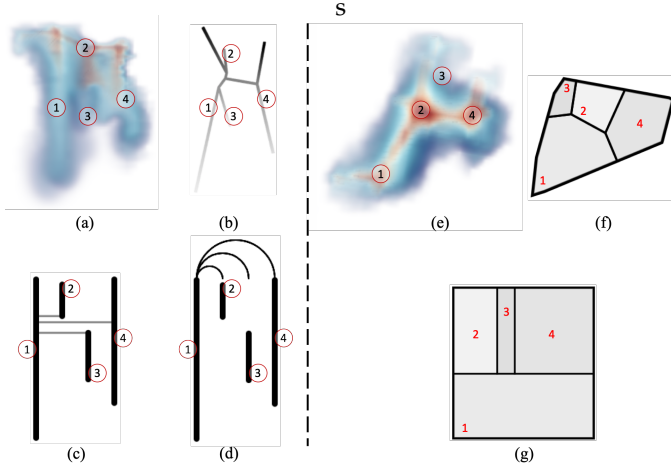


Fig. 10: We showcase glyph designs of a finger. The same numbers label corresponding branches. The left four views display side views of the finger. (a) shows the side view of the finger volume. (b) is the identified skeleton of the finger. The linear glyph (c) displays connections between branches of the finger. When horizontal connections are too close or even overlap, the alternative design (d) shows the tree structure with less ambiguity than (c). Right three views display top views of the finger. (e) is the top view of the finger volume. The Voronoi glyph (f) is shown on the spatial projection panel; Voronoi cells that are inside the convex hull are corresponding to the finger branches. The rectangular glyph (g) is for contrasting the topological complexity between the finger branches on the tracking graphs.

topological complexity of finger structures; more complex fingers have wider space for drawing. Users can switch the style of the glyph between the linear glyph (Fig. 9f) and the rectangular glyph (Fig. 11) to observe different facets of fingers. In addition, users can click on a particular glyph to observe the details of the corresponding finger in the volume and skeleton views. Also, users can choose to filter out short fingers for this view if tracking persistent fingers is preferred. Below we describe the tracking graph in more detail, including the generation of geometric glyphs for showing structures of fingers, the color encoding of links for evolutionary events of fingers, the minimization of link crossings for reduction of visual clutter, and the interactions for exploration of temporal events.

6.4.1 Linear Glyph for Finger Side View

To display the evolution of geometric structures of fingers, we enhance tracking graphs by nesting geometry-driven glyphs on the tracking graphs. In Fig. 9f, for the side view of fingers, we draw finger branches and their connections in a plane with minimized occlusion and also preserve the height of branches according to the requirements of the earth scientist. Two possible solutions are discussed in the following.

Projection We may project finger skeletons onto a plane. However, the traditional orthogonal projection suffers from edge crossing problems. To remedy the edge crossing for the projection of tree-like structures, Marino

and Kaufman [43] produced radial planar embeddings of the structures. However, fingers are vertical objects, and radial planar embeddings of fingers may lose the height information. Although the method of Marino and Kaufman [43] is good at preserving the curvature of 3D objects, the curvature is not an essential feature of fingers.

Tree drawing We draw fingers as linear glyphs. Heine et al. [37] proposed a graph-drawing method to plot branches of contour trees in a plane with minimized edge crossings. The method of Heine et al. [37] represents branches by vertical lines and denotes links between branches by horizontal lines. Heights of branches and connections between branches are shown clearly in the results of this method. Thus, we augment the tree-drawing method of Heine et al. [37] to display the side view of fingers such as Fig. 10c. Note that, although trees are planar graphs, crossings of tree edges are inevitable for some instances in this design; the reason is that only the x -axis is free to arrange tree branches, and the y -axis is used to encode the height of branches. We draw the longest branch of a finger at the leftmost of the glyph so that we can locate the principal branch quickly. Users can choose to encode change of densities along branches by using the gradient darkness of vertical lines such as Fig. 5c. When hovering over a linear glyph on the tracking graph, connections between branches of this finger become arcs hanging at the top of the glyph to reduce visual clutter, such as Fig. 10d. The results of the tree-drawing method are abstract forms of fingers, and display the height and connections of branches effectively.

6.4.2 Rectangular Glyph for Finger Top View

In Fig. 11, we draw the top view of fingers, and display quantitative attributes and relative positions of fingers by using treemap based rectangular glyphs. The treemap technique was proposed by Johnson and Shneiderman [44], who mapped elements onto a rectangular region in a space-filling manner and displayed quantity values of elements effectively. Wood and Dykes [45] developed spatially ordered treemap by extending squarified treemaps [46] to incorporate spatial information of elements. We use the spatially ordered treemap [45] to generate rectangular glyphs for finger branches, as shown in Fig. 10g. Each branch is represented by a rectangle on the glyphs. Areas of rectangles encode one of the numeric attributes of branches, including statistics or topological measurements; in this work, the area encodes the topological complexity of branches defined in Sect. 6.2 by default. The rectangles of branches are arranged based on both the spatial proximity and the balance of aspect ratio. Moreover, to compare fingers in the tracking graph and assign more space for topologically complex fingers, we encode the size of rectangles of whole fingers by the topological complexity of fingers. The *topological complexity of a finger* is defined by the number of critical points on the finger skeleton; intuitively, a finger has more critical points, usually indicates this finger has more branches and hence is more complex in its topological structure.

6.4.3 Link Encoding for Evolutionary Events of Fingers

We use links to represent the temporal relationships between fingers. Fingers between adjacent timesteps are related in Sect. 5.4. When time varies, fingers may grow, merge

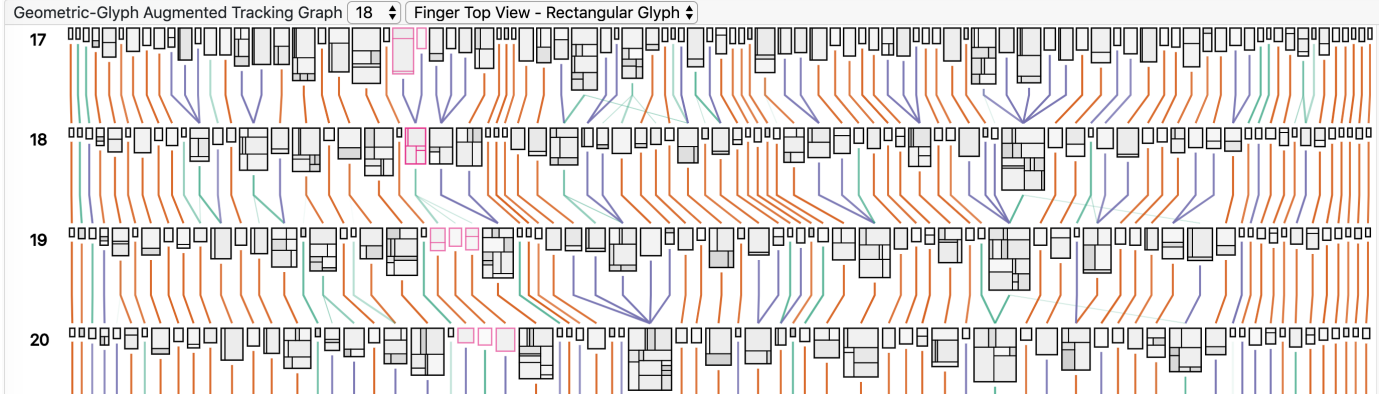


Fig. 11: We display the geometric-glyph augmented tracking graph with rectangular glyphs. A finger associated with merging and splitting events at timestep 18 is highlighted by red-violet and analyzed in Fig. 14 further.

with other fingers, or split into multiple fingers. To indicate these three types of the evolution of fingers, we use three different hues of links following the qualitative color advice of ColorBrewer [47].

Brown Link Brown links indicate that fingers grow with minor changes between consecutive timesteps. Specifically, at least seventy-five percent volume of the finger is preserved in one of the connected fingers at the subsequent timestep.

Blue Link A blue link indicates the case when multiple fingers merge into one finger at the subsequent timesteps. Specifically, the finger at the subsequent timestep incorporates seventy-five percent volume of each of the fingers at the previous timestep.

Green Link A green link indicates that a finger splits into multiple fingers at the subsequent timestep, and none of the fingers at the subsequent timestep have seventy-five percent volume of the finger at the previous timestep.

We use the opacity of links to encode link weights; the *weight of each link* is the size of the overlapping volume between linked fingers. If fingers have weak connections, their links are almost transparent so that visual clutter is reduced.

6.4.4 Iterative Minimization of Link Crossings

We reduce link crossings to alleviate the visual clutter of the tracking graphs. Since links between fingers are weighted, the reduction of link crossings in our application is a graph drawing problem: edge crossing minimization for weighted bipartite graphs. Çakıroğlu et al. [48] enhanced and tested five heuristic methods for this graph drawing problem, and concluded that W-GRE [48], [49] and W-PM [48], [50] methods produce the best results. Hence, we utilize W-GRE method in our application to minimize intersections of weighted links.

We propose a W-GRE based iterative algorithm for the crossing minimization, which arranges fingers of each row iteratively until obtaining a good result. We describe the algorithm in the following.

Step 1 The fingers in the first row are arranged by the ascending order of their x coordinates initially.

Step 2 We order fingers from the second row to the last row.

We minimize the crossings of the links between a given row and its previous row by using the W-GRE method.

Step 3 We order fingers from the last but one row to the first row.

We minimize the crossings of the links between a given row and its following row by using the W-GRE method.

Step 4 Repeat Step 2 and Step 3 to order the fingers of each row until reaching the convergence of the finger order.

Usually, repeating two times can produce a good result in our experiments.

6.4.5 Interactive Finger Tracking

We offer three interactions for scientists to track fingers effectively.

Scientists can click on a finger of interest from the tracking graphs to select the finger. Then, the selected finger and the other related fingers are highlighted in the tracking graphs by coloring the backgrounds of the fingers in Fig. 9f or the strokes in Fig. 11. Hence, users can follow the evolution of fingers efficiently.

The earth scientist is also interested in tracking the volume of a finger. Note that each link is associated with the overlapping volume between temporally related fingers. Users can click on a finger of interest first and click on associated links to observe overlapping volume between this finger of interest and one of its connected fingers in the finger volume view, which is illustrated in Sect. 7.3 and Fig. 14 in detail.

Furthermore, the earth scientist requires designs to track branches. If a complex finger separates into multiple smaller fingers over time, it is essential to know each branch of the complex finger comes to which smaller finger entity afterwards; also, if multiple fingers fuse into a complex finger, it is important to understand the correspondence between the individual fingers and the branches that they got merged to. On our tracking graph, we identify corresponding branches between linked fingers interactively. Having identified temporally relevant branches in Sect. 5.4, when hovering over a link between two connected fingers, the relevant branches between the fingers are highlighted by the red-violet color on glyphs as shown in Fig. 14.

7 CASE STUDY AND EXPERT FEEDBACK

Earth scientists used our geometry-driven visual-analytics system to explore the phenomena of viscous and gravitational fingering and perform domain-specific tasks. After we have built the visual-analytics system, we discussed our work with the earth scientist. The earth scientist and his graduate student both thought that this work provides a new perspective to analyze viscous and gravitational fingering. They acknowledged that the extraction of fingers in this way is effective and that the minimal occlusion leads to a clear representation of the fingers. The earth scientists also gave us valuable suggestions about our system. Below we discuss several use cases that were studied using our system.

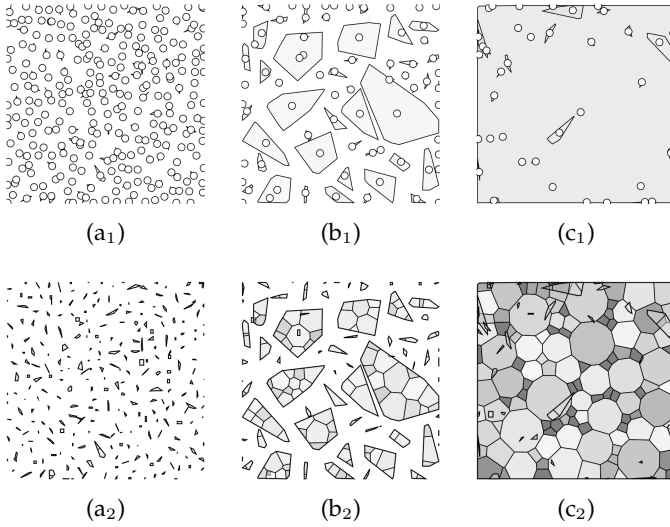


Fig. 12: There are three important phases for the evolution of fingers: (a) the onset phase, (b) the growth phase, and (c) the termination phase. Convex hulls of (a₁), (b₁), and (c₁) display the spatial coverage of individual fingers. Voronoi glyphs of (a₂), (b₂), and (c₂) show finger branches.

7.1 Case 1: Recognition of Evolutionary Phases

According to the earth scientists, the evolution of the instability may have (at least) three important phases: onset, growth, and termination, which have also been studied in previous works [2], [12], [13]. The earth scientists identified the three phases based on the spatial projection panel. In the onset phase identified in Fig. 12a, the instability is triggered, and the displacement front breaks up into many small-scale fingers. After the onset phase, the dense fingers grow non-linearly and penetrate the underlying lighter fluid. In Fig. 12b, many medium-sized fingers form in this growth phase. These medium-sized fingers grow, merge, and/or split over time. Eventually, multiple fingers merge to form a few ‘mega-plumes’ that span most of the reservoir, as shown in Fig. 12c. Once those fingers reach the bottom of the domain, the instability shuts down or terminates.

7.2 Case 2: Identification of Fingers in 3D Space

Because the existing methods do not capture the geometric structures of fingers, the earth scientists mentioned the difficulty in tracking density patterns of fingers in 3D space, due

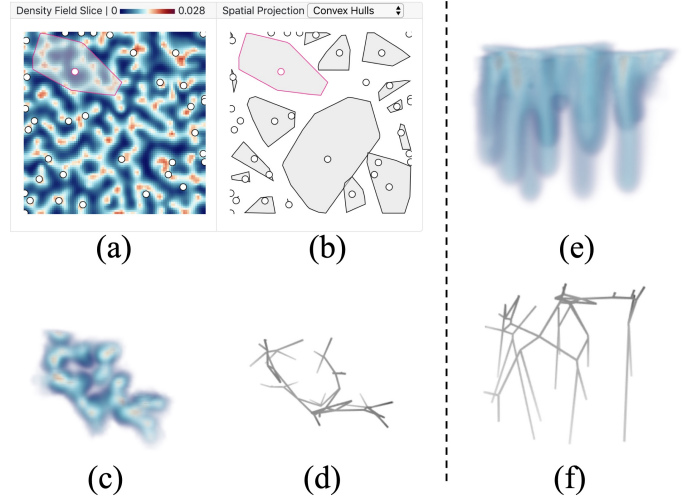


Fig. 13: The earth scientists identified a finger of interest from (b) the spatial projection panel. Then, they observed the high-density hexagons under the convex hull of the finger in (a) the density field slice view. They further confirmed the correspondence between (c) the top view of the finger volume and the hexagons in (a). Also, they found the finger skeleton (d) preserved the geometric structure of (c). Next, they looked at the side view of the finger volume (e) but felt difficult for observing finger branches due to the occlusion. They then interacted with the 3D skeleton (f) and obtained how these branches form in space over time.

to occlusion. There are two problems. The first is to identify where finger branches are in space. After the identification of finger branches, the second problem is to understand how the CO₂ volume flows spatio-temporally, and comprehend how the hexagonal sheets in the top (e.g., Fig. 13cd) split and develop into columnar fingers (e.g., Fig. 13ef) below. Specifically, given hexagonal cells (e.g., Fig. 13cd), it is important to know that whether fingers tend to form along with the boundaries of hexagonal cells or form below centers of the hexagonal cells. By using our system, the earth scientists started solving the problems.

To identify where are finger branches, the scientists first looked at the density field slice view and spatial projection view. The earth scientists thought projection points added on the density field slice view, Fig. 13a, is an effective addition to traditional density-slice views, and allows them to identify finger locations on any slice with the corresponding hexagonal features at the slice. Furthermore, from the spatial projection panel, Fig. 13b, the earth scientists found two fingers that occupy a large space. They clicked on one of the two for analysis, and the convex hull of the finger was superimposed on the density field slice view, Fig. 13a. They focused on the high-density hexagons under the convex hull in the slice view, and adjusted the z -value slider of Fig. 9a to understand the change of densities along the z coordinate. Note that the finger volume (Fig. 13ce) and skeleton (Fig. 13df) views were displayed after the selection of the finger. They verified the correspondence between the hexagons under the convex hull in Fig. 13a and the top view of the volume, Fig. 13c. Next, they confirmed the correspon-

dence between the finger volume and skeleton. The skeleton Fig. 13d captured the structure of the volume Fig. 13c. Afterwards, they rotated finger volume and skeleton to see side views of the finger. The finger branches occluded severely in the volume visualization Fig. 13e. However, when interacting with the skeleton Fig. 13f, they could intuitively acquire the geometric structures of the finger and identify finger branches in space.

To understand how CO₂ volume flows in space and how fingers form in time, since the finger results from that the CO₂ flows over time, the finger skeleton at a timestep (Fig. 13f) approximates the flowing track of CO₂ over time; hence, the earth scientists could answer whether the high-density hexagons form this finger over time, and understand how these branches form. Specifically, based on the finger skeletons, Fig. 13f, the experts obtained an insight that the fingers usually form along the boundaries of hexagonal cells instead of forming below centers of hexagonal cells.

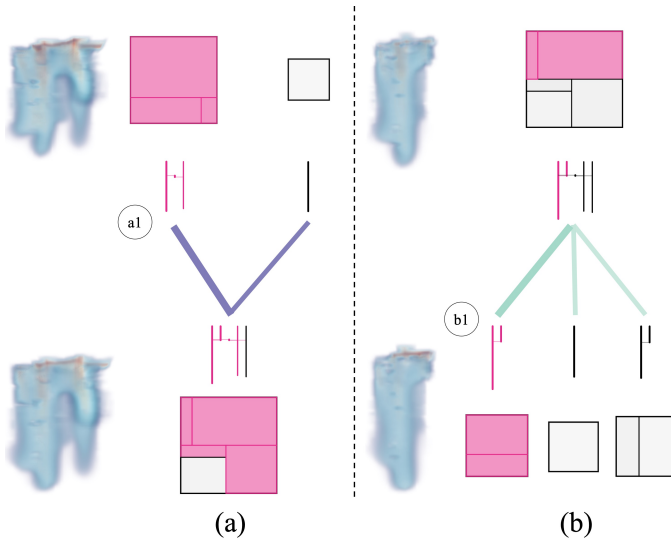


Fig. 14: After evolving one timestep, (a) fingers may merge into a complex finger, or (b) a complex finger may split into more fingers. To track branches, users can hover over a link; the link becomes thick, and associated branches on glyphs are highlighted by red-violet color. To track the volume of fingers, users can click on a link; then, the overlapping volume between linked fingers is shown to be compared.

7.3 Case 3: Exploration of Finger Evolution

The earth scientists identified the growth, merging, and splitting events of fingers over time from the geometric-glyph augmented tracking graph. First, we illustrated the encodings of our designs to the earth scientists. After we explained the three colors used to represent the growing, merging, and splitting of the fingers, they appreciated how the tracking graph could provide insights into the temporal evolution of the fingers. We next explained the two kinds of finger glyphs to the earth scientists. Compared with previous tracking graphs that only use dots to represent fingers, the geometric glyphs of our tracking graphs offered more details and facets of fingers to the earth scientists. With respect to the linear glyphs (e.g., Fig. 10c), at first glance,

they were confused with the encoding of horizontal lines initially. However, after we explained that the horizontal lines are used to represent connections between vertical branches, they were able to understand the structures and thought that this design is effective. They thought drawing fingers in a plane would cause distortion, but found that the branches and their connections are shown clearly, and it is easy to count the number of vertical branches. In regards to the rectangular glyphs (e.g., Fig. 10g), the expert was able to comprehend and quickly count the number of complex branches. Also, they suggested highlighting the correspondence between the rectangles and the branches in the volume so that they can understand how the structures of fingers from the glyphs well.

We illustrate how the earth scientists analyzed the evolution of fingers and branches by using our system. First, they found a finger of interest with merging and splitting events, which is highlighted by red-violet in Fig. 11 and extracted in Fig. 14. Concentrating on this finger, they hovered on the left link above the merged finger (Fig. 14a), and hovered on the leftmost link below the finger (Fig. 14b) to track corresponding branches that were highlighted by red-violet in glyphs. The corresponding linear glyphs and rectangular glyphs between consecutive timesteps were found to be consistent. To track the volume, they first clicked on (a1) the upper-left finger of Fig. 14a to look at its volume; then, they clicked on the merged finger at the next timestep and clicked on the link to (a1) to observe the partial volume of the merged finger that comes from (a1). The two volume images are shown on the left of Fig. 14a, and the change of the volume was observed. Similarly, they tracked the overlapping volume of fingers in Fig. 14b, and observed that the corresponding branches grow longer. After using our system, the earth scientists thought our tracking graphs are valuable to identify when and where the fingers grow, merge, and split over time. By compared with the previous works which do not construct branches of fingers explicitly, our methods track finger branches more efficiently.

8 DISCUSSION

Sensitivity of the finger core detection If the quality of data is low, for example, resulting from noise or coarse discretization, the approximation of derivatives usually has high errors. Since the ridge-voxel detection is based on the approximated derivatives, the ridge-guided extraction of finger cores usually also has high errors. Also, if the density fields are not smooth enough, the detected ridge structures are likely broken, which may lead to disconnected finger branches. In this application, when finger branches are disconnected unexpectedly, we adjust a spacing parameter h to incorporate more voxels into finger cores to acquire more connected features; the details are illustrated in App. B.

Height value selection for the top layer We select a fixed height value as the separation between the top layer and the bottom layer of the whole domain for the segmentation in Sect. 5.2 by following the previous works [5], [11], [13]. Physically, the top layer initially grows diffusively in time, i.e., as the square root of time, which is much slower than the convective time scale over which the fingers grow. Once the instability is triggered, this diffusive boundary

layer thins. Since the top layer is varying in nature, one limitation of using a fixed height value for the top layer is that the fixed height value may not be suitable for all conditions. However, given the domain height ranging from 40 to 0 in this application, we find that the fingers are separated well throughout all timesteps for a fixed height value of 38. For other datasets, our system provides visualizations for scientists to identify a suitable value.

Scalability of the tracking graph By given a screen resolution of 2880×1800 , the geometric-glyph augmented tracking graph supports displaying around one hundred fingers and hundreds of branches for each timestep and showing four timesteps when placed in our visual-analytics system. If there are more fingers at a timestep, it becomes hard to arrange all the fingers at a timestep in the same row by using our tested screen resolution. To remedy this scalability issue, a larger screen, more simplification of finger representations, and allowing multi-level exploration of fingers may be helpful.

Value of the visual-analytics system The visual-analytics system helps scientists acquire the 3D geometric properties including branches in space and branching behaviors in time efficiently and effectively, to relieve cumbersome work for the geometric analyses of fingers by hand. Also, specific geometric measures, including finger widths and fingertip locations, can be directly derived from the finger skeletons. Moreover, the branch tracking offered by our system is new and not directly available by using previous methods [5], [11], [12], [13].

Future works We identify future works from the interactions with the earth scientists. First, our collaboration with the earth scientists is ongoing to use the visualization and analysis tools developed in this work to study the scaling behavior associated with pattern formation in flow instabilities. Specifically, the topological measurements offered by our methods, including the number of branches and the number of critical points, can be studied for discovering new scaling laws. Second, the 3D cube in the depth selection panel, Fig. 9a, can be enhanced to display the selected finger in 3D space by using wired structures. Third, we may add an iso-contour view to observe and track the iso-contours of the scalar fields. Fourth, a line chart to display the number of merging and splitting events over time is essential for the temporal analysis of fingers and associated mixing and spreading processes of, e.g., CO₂ or contaminants.

9 CONCLUSION

In this paper, we present a novel geometry-driven approach with a new ridge voxel guided finger core detection, a finger skeletonization and trim method, and a spanning tree based finger branch extraction method for the detection of viscous and gravitational fingering. An interactive visual-analytics system with a novel geometric-glyph augmented tracking graph is established for domain scientists to track the geometric growth, merging, and splitting of fingers over time in detail. The earth scientists recognized the value of our work and thought that this could reduce their analysis workload both in space and time significantly.

APPENDIX A

DERIVATIVE APPROXIMATION FOR RIDGE Voxel DETECTION

Let the raw density function of the input field noted by $g(x, y, z)$. In Fig. 15, the blue points represent midpoints of voxels. We assume density values at blue points are the exact values of voxels. In this work, we approximate derivatives of $g(x, y, z)$ by two alternative methods as follows. Without the loss of generality, we illustrate how to estimate the derivatives at the red-circled point, $\mathbf{p}_0 = (x_0, y_0, z_0)$, of Fig. 15.

Method One We take the estimation of the partial derivative with respect to x coordinate (i.e., the r_x term of Equation 1) at the red-circled point as an example. The adjacent two orange points in Fig. 15a are h units away from the red-circled midpoint \mathbf{p}_0 along the x coordinate; the density values of the two orange points are $g(x_0 + h, y_0, z_0)$ and $g(x_0 - h, y_0, z_0)$ respectively. Then, we use the central difference formula to estimate the derivative at \mathbf{p}_0 :

$$\begin{aligned} r_x &\approx g_x(\mathbf{p}_0, h) \\ &= g_x(x_0, y_0, z_0, h) \\ &= \frac{g(x_0 + h, y_0, z_0) - g(x_0 - h, y_0, z_0)}{2h} \end{aligned} \quad (7)$$

Let s be the voxel size (i.e., the length of the side of the voxel). When h is equal to s , the orange points overlap with two adjacent blue points of the red-circled point. Hence, we use densities at the two adjacent blue points directly to estimate the partial derivative with respect to x ; namely, we let h equal s for Equation 7 to acquire the partial derivative. Partial derivatives for other coordinates are estimated similarly by using their corresponding central differences and letting h equal s . The result is shown in the leftmost column of Fig. 16.

Method Two We also test the facet model [51] which approximates coefficients of the Taylor polynomial locally by using least squares method. We use the Taylor polynomial f , Equation 3, to approximate the function g near the red-circled point \mathbf{p}_0 of Fig. 15b locally. The unknown parameters are the terms of $J(\mathbf{p}_0)$ in Equation 1 and the elements of $H(\mathbf{p}_0)$ in Equation 2. In Fig. 15b, given the densities of the blue points near the red-circled point, to acquire the unknown parameters, we use the least squares method to optimize the following function:

$$\text{minimize } \sum_{\mathbf{p} \in \mathcal{P}} (f(\mathbf{p}) - g(\mathbf{p}))^2 \quad (8)$$

where \mathcal{P} is a set of midpoints that are close to the red-circled point \mathbf{p}_0 . The results of this method for the finger core extraction are displayed in the rightmost column of Fig. 16.

Results on synthetic data We test both the methods mentioned above on synthetic data. The volume rendering of the synthetic data is shown in Fig. 18. The columnar and spiral shapes have higher densities in their central regions. The results for the two methods on this data are shown in the leftmost and rightmost of Fig. 17 respectively. Method One, when h equals s , produces curvilinear features that are similar to the facet model (Method Two); these curvilinear features are confirmed to be ridge voxels.

Summary From this study, it is observed Method One, when h equals s , and Method Two are both able to extract ridge voxels from the synthetic data (Fig. 17). However, for the fingering data, the finger cores produced by Method One in Fig 16 are more continuous than the finger cores detected by Method Two, the facet model. Hence, in our system, we use Method One as the default technique for the extraction of finger cores.

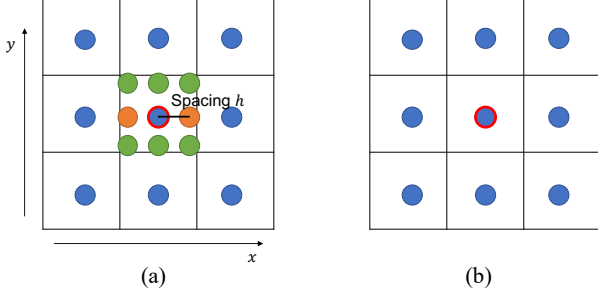


Fig. 15: The two illustration figures (a) (for Method One) and (b) (for Method Two) are used to help elucidate the two derivative approximation methods in App. A.

APPENDIX B

EFFECT OF CHANGING h FOR RIDGE Voxel GUIDED EXTRACTION OF FINGER CORES

Method One of App. A fixes h to be the voxel size s and acquires ridge voxels. However, if we use the ridge voxels directly to be the finger cores in this application, specific branching structures of fingers may be missing, which is shown in the leftmost of Fig 16. According to the study of Damon [34], ridges do not represent branching structures well theoretically, and the branching structures may be close spatially but disconnected when represented by ridges. To remedy this for this application, we acquire more connections of finger branches by incorporating more voxels that are near ridges in finger cores; to implement this idea, we adjust the spacing parameter h for the extraction of finger cores as follows. When h is smaller than s , we estimate the densities of the orange points in Fig. 15a through the tri-linear interpolation of densities of nearby blue points. The results with varying values of h for finger core extraction are shown on the left side of Fig 16. Intuitively, when h is equal to s , the extracted thin features are ridge voxels; when h becomes smaller than s , the resulting features become thick by expanding from ridge voxels to preserve more branching connections. The same phenomenon is observed for the synthetic data in Fig. 17 as well. The adjustment of h is flexible for the finger extraction because domain scientists can control the values of h to acquire finger cores by trading off thickness against more branching connections of structures. In our paper, we use a small value of h (i.e., 10^{-5}) by default to extract finger cores to preserve more branching connections; also, the extracted thick finger cores are close to the complete volume of fingers, which is beneficial for the extraction of full fingers. We further use the Reeb graph based skeletonization to acquire thin skeletons.

We offer the theoretical analysis for the spacing parameter h hereafter. When changing h , we examine how the estimated terms in the Jacobian matrix (Equation 1) and the Hessian matrix (Equation 2) change accordingly. Finally, we conclude what specific structures are extracted by using different h values. We discuss the situations when h is smaller than s and larger than 0 in the following.

B.1 Effect of h for Jacobian Matrix

Given the center of a voxel, $\mathbf{p}_0 = (x_0, y_0, z_0)$, the Jacobian matrix $J(\mathbf{p}_0)$ of Equation 1 is represented by $\hat{J}(\mathbf{p}_0, h)$ with an additional parameter h which is given by

$$\hat{J}(\mathbf{p}_0, h) = (g_x(\mathbf{p}_0, h), g_y(\mathbf{p}_0, h), g_z(\mathbf{p}_0, h))^T \quad (9)$$

When changing h , we analyze how the three components of $\hat{J}(\mathbf{p}_0, h)$ change. Without loss of generality, we examine how the component $g_x(\mathbf{p}_0, h)$ changes hereafter, where $g_x(\mathbf{p}_0, h)$ is defined by Equation 7. When h equals s , $g_x(\mathbf{p}_0, h) = g_x(\mathbf{p}_0, s) = g_x(x_0, y_0, z_0, s)$. Next, we identify the relationship between $g_x(\mathbf{p}_0, s)$ and $g_x(\mathbf{p}_0, h)$ when $h \in (0, s)$. Note that, for all $h \in (0, s)$, $g(x_0 \pm h, y_0, z_0)$ are represented by the tri-linear interpolation between $g(x_0, y_0, z_0)$ and $g(x_0 \pm s, y_0, z_0)$. We represent $g(x_0 \pm h, y_0, z_0)$ by polynomials of $g(x_0, y_0, z_0)$ and $g(x_0 \pm s, y_0, z_0)$ through the formula of the tri-linear interpolation; we substitute the polynomials into Equation 7 and obtain that, $\forall h \in (0, s]$,

$$g_x(x_0, y_0, z_0, h) = g_x(x_0, y_0, z_0, s) \quad (10)$$

Hence, $\forall h \in (0, s]$,

$$\hat{J}(\mathbf{p}_0, h) = \hat{J}(\mathbf{p}_0, s) \quad (11)$$

In other words, no matter what value of $h \in (0, s]$ that we use, the Jacobian matrix $\hat{J}(\mathbf{p}_0, h)$ does not change.

B.2 Effect of h for Hessian Matrix

We use $\hat{H}(\mathbf{p}_0, h)$ to represent the Hessian matrix $H(\mathbf{p}_0)$ of Equation 2, where $\hat{H}(\mathbf{p}_0, h)$ is defined by

$$\hat{H}(\mathbf{p}_0, h) = \begin{bmatrix} g_{xx}(\mathbf{p}_0, h) & g_{xy}(\mathbf{p}_0, h) & g_{xz}(\mathbf{p}_0, h) \\ g_{yx}(\mathbf{p}_0, h) & g_{yy}(\mathbf{p}_0, h) & g_{yz}(\mathbf{p}_0, h) \\ g_{zx}(\mathbf{p}_0, h) & g_{zy}(\mathbf{p}_0, h) & g_{zz}(\mathbf{p}_0, h) \end{bmatrix} \quad (12)$$

Similar to the mathematical analysis of the Jacobian matrix $\hat{J}(\mathbf{p}_0, h)$, we analyze how the terms of $\hat{H}(\mathbf{p}_0, h)$ change when h varies. Without loss of generality, we examine how the terms $g_{xx}(\mathbf{p}_0, h)$ and $g_{xy}(\mathbf{p}_0, h)$ change hereafter. The central difference formula for $g_{xx}(\mathbf{p}_0, h)$ is given by

$$\begin{aligned} g_{xx}(\mathbf{p}_0, h) &= g_{xx}(x_0, y_0, z_0, h) \\ &= \frac{g(x_0 + h, y_0, z_0) - 2g(x_0, y_0, z_0) + g(x_0 - h, y_0, z_0)}{h^2} \end{aligned} \quad (13)$$

We represent $g(x_0 \pm h, y_0, z_0)$ by polynomials of $g(x_0, y_0, z_0)$ and $g(x_0 \pm s, y_0, z_0)$ through the formula of the tri-linear interpolation, and obtain that, $\forall h \in (0, s]$,

$$g_{xx}(x_0, y_0, z_0, h) = \frac{s}{h} g_{xx}(x_0, y_0, z_0, s) \quad (14)$$

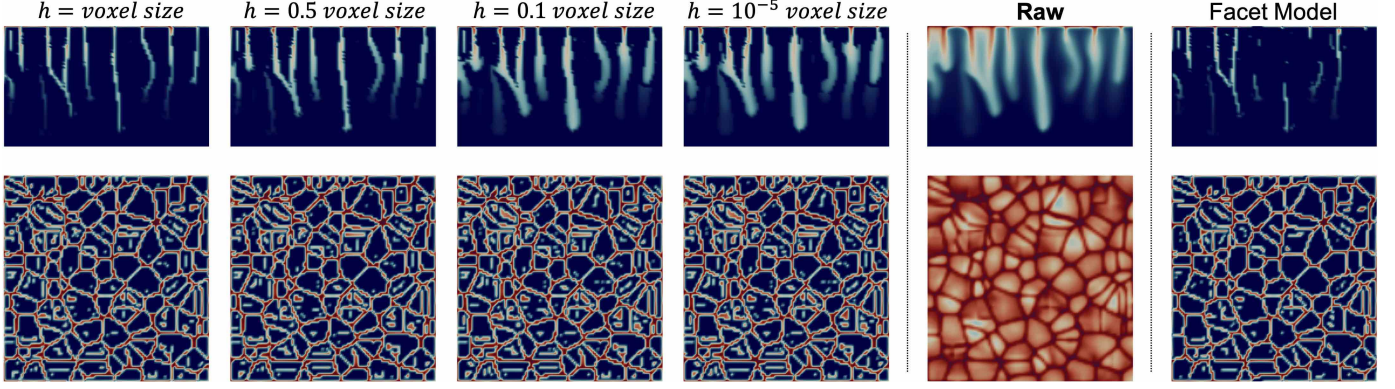


Fig. 16: We display results of Method One with varying h values and Method Two for the fingering data. The first row is for the side view, and the second row is for the top view.

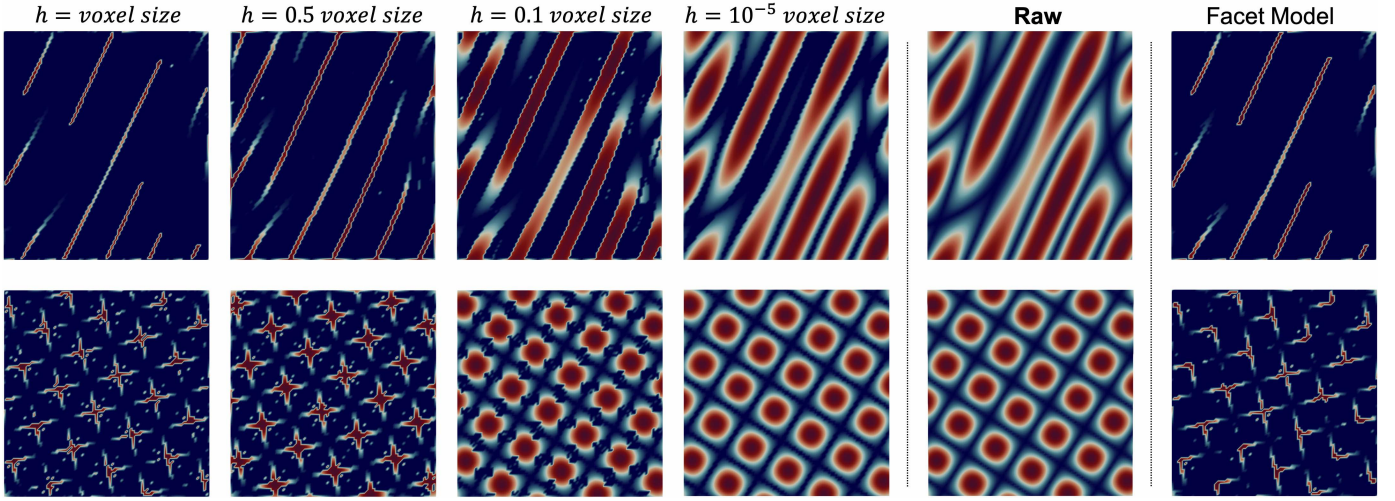


Fig. 17: We display results of Method One with varying h values and Method Two for synthetic data. The first row is for the side view of Fig 18, and the second row is for the top view.

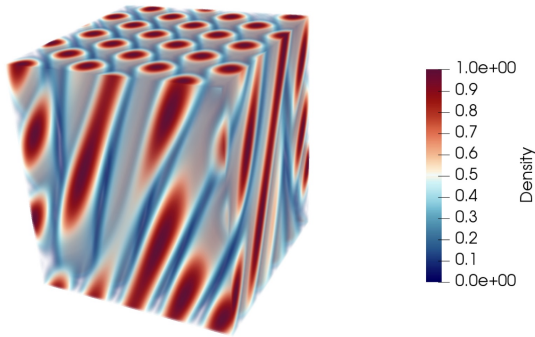


Fig. 18: This figure shows the volume rendering image of the synthetic data, which is consisting of columnar and spiral shapes with high-density central regions.

The central difference formula for $g_{xy}(\mathbf{p}_0, h)$ is given by

$$\begin{aligned}
 g_{xy}(\mathbf{p}_0, h) &= g_{xy}(x_0, y_0, z_0, h) \\
 &= (g(x_0 + h, y_0 + h, z_0) - g(x_0 + h, y_0 - h, z_0) \\
 &\quad - g(x_0 - h, y_0 + h, z_0) \\
 &\quad + g(x_0 - h, y_0 - h, z_0)) / (4h^2)
 \end{aligned} \tag{15}$$

We represent $g(x_0 \pm h, y_0 \pm h, z_0)$ by polynomials of $g(x_0, y_0, z_0)$ and $g(x_0 \pm s, y_0 \pm s, z_0)$ through the rules of the tri-linear interpolation, and obtain that, $\forall h \in (0, s]$,

$$g_{xy}(x_0, y_0, z_0, h) = \frac{s}{h} g_{xy}(x_0, y_0, z_0, s) \tag{16}$$

Hence, $\forall h \in (0, s]$,

$$\hat{H}(\mathbf{p}_0, h) = \frac{s}{h} \hat{H}(\mathbf{p}_0, s) \tag{17}$$

In other words, the Hessian matrix $\hat{H}(\mathbf{p}_0, h)$ is equal to $\hat{H}(\mathbf{p}_0, s)$ scaled by $\frac{s}{h}$. Therefore, the eigenvalues of $\hat{H}(\mathbf{p}_0, h)$ are equal to the eigenvalues of $\hat{H}(\mathbf{p}_0, s)$ scaled by $\frac{s}{h}$ for all $h \in (0, s]$; the eigenvectors of $\hat{H}(\mathbf{p}_0, h)$ remain the same.

B.3 Effect of h for Ridge Criterion

We analyze the effect of h for Condition One and Two of Lindeberg's criterion [25] demonstrated in Sect. 5.1 as follows.

B.3.1 Effect of h for Condition One

We first analyze Condition One. Note that the eigenvalues of $\hat{H}(\mathbf{p}_0, h)$ are equal to the eigenvalues of $\hat{H}(\mathbf{p}_0, s)$ scaled

by $\frac{s}{h}$ through Equation 17, and the scaling value $\frac{s}{h}$ is positive. Hence, if the eigenvalues of $\hat{H}(\mathbf{p}_0, s)$ are smaller than zero, the eigenvalues of $\hat{H}(\mathbf{p}_0, h)$, $\forall h \in (0, s]$, must be also smaller than zero, and vice versa. In other words, if certain voxels that satisfy Condition One when $h = s$, then these voxels also satisfy Condition One when $h \in (0, s]$, and vice versa.

B.3.2 Effect of h for Condition Two

For Condition Two, we use $\hat{d}_i(\mathbf{p}, h)$ to represent the $d_i(\mathbf{p})$ of Equation 6, where $\hat{d}_i(\mathbf{p}, h)$ is defined by

$$\hat{d}_i(\mathbf{p}, h) = \vec{v}_i^T \hat{J}(\mathbf{p}, h), \quad i = 1, 2 \quad (18)$$

Through Equation 4, we have

$$\hat{d}_i(\mathbf{p}, h) = \vec{v}_i^T (\hat{J}(\mathbf{p}_0, h) + \hat{H}(\mathbf{p}_0, h) \cdot \Delta \mathbf{p}(h)), \quad i = 1, 2 \quad (19)$$

We examine whether exists a feature point $\mathbf{p}_1(h) = (x_1(h), y_1(h), z_1(h))^T$ within the given voxel. $\Delta \mathbf{p}_1(h)$ is the displacement of the feature point $\mathbf{p}_1(h)$ to the center point \mathbf{p}_0 when h varies, and is given by $\Delta \mathbf{p}_1(h) = \mathbf{p}_1(h) - \mathbf{p}_0$. According to Condition Two, we let $\hat{d}_i(\mathbf{p}_1, h) = 0$, $i = 1, 2$. Then, by transforming Equation 19, $\Delta \mathbf{p}_1(h)$ satisfies that

$$\vec{v}_i^T \hat{H}(\mathbf{p}_0, h) \cdot \Delta \mathbf{p}_1(h) = -\vec{v}_i^T \hat{J}(\mathbf{p}_0, h), \quad i = 1, 2 \quad (20)$$

We substitute Equation 11 and Equation 17 into Equation 20, and $\Delta \mathbf{p}_1(h)$ satisfies that

$$\vec{v}_i^T \hat{H}(\mathbf{p}_0, s) \cdot \left(\frac{s}{h} \Delta \mathbf{p}_1(h)\right) = -\vec{v}_i^T \hat{J}(\mathbf{p}_0, s), \quad i = 1, 2 \quad (21)$$

Note that, let h be s for Equation 20, and $\Delta \mathbf{p}_1(s)$ satisfies the following equation

$$\vec{v}_i^T \hat{H}(\mathbf{p}_0, s) \cdot \Delta \mathbf{p}_1(s) = -\vec{v}_i^T \hat{J}(\mathbf{p}_0, s), \quad i = 1, 2 \quad (22)$$

Hence, by comparing the above two equations, Equation 21 and 22, we have

$$\Delta \mathbf{p}_1(h) = \frac{h}{s} \Delta \mathbf{p}_1(s) \quad (23)$$

In other words, when h is smaller than s , the feature displacement $\Delta \mathbf{p}_1(h)$ is equal to the feature displacement $\Delta \mathbf{p}_1(s)$ scaled by $\frac{h}{s}$, where $\frac{h}{s} < 1$. Condition Two requires the feature point $\mathbf{p}_1(h) = \mathbf{p}_0 + \Delta \mathbf{p}_1(h)$ to be within or on the boundary of the voxel that is centered at \mathbf{p}_0 and has size s . Because $\mathbf{p}_1(s) = \mathbf{p}_0 + \Delta \mathbf{p}_1(s) = \mathbf{p}_0 + \frac{s}{h} \Delta \mathbf{p}_1(h)$ through Equation 23, this condition is equivalent to require the ridge point $\mathbf{p}_1(s)$ to be within or on the boundary of a cube that is centered at \mathbf{p}_0 and has size $\frac{s}{h} \cdot s = \frac{s^2}{h}$. Hence, when using a smaller h , the cube size $\frac{s^2}{h}$ becomes larger, and so, it is more likely to find satisfied ridge points.

B.4 Discussion for h

From the analyses above, therefore, we obtain thicker finger cores and acquire more connections of branches when using a smaller h . When h approaches 0, Condition Two becomes weak, and we tend to extract all voxels that satisfy Condition One. In other words, we tend to extract voxels, whose the second-order directional derivatives along the two eigenvectors, v_1 and v_2 , are smaller than zero (i.e.,

where the density function is concave down along the two eigenvectors), as finger cores.

Compared with density thresholding Although the meaning of h is less intuitive than the density threshold, the effect of h for the extraction of finger cores is apparent: when h becomes smaller, the extracted finger cores become thicker, and more connections between branches are acquired. Moreover, when using a hard density threshold, the preservation of the low-density fingertips and branches contradicts the good separation of fingers. However, when using h as a parameter, we can obtain both of them. High h preserves low-density fingertips and acquires well-separated structures. To obtain more connected features, we choose to lower the h .

ACKNOWLEDGMENTS

We thank Yujia Wang and Junpeng Wang for providing design suggestions for the geometric-glyph augmented tracking graph. This work was supported in part by UT-Battelle LLC 4000159557, Los Alamos National Laboratory Contract 471415, and NSF grant SBE-1738502.

REFERENCES

- [1] J. Moortgat, "Viscous and gravitational fingering in multiphase compositional and compressible flow," *Advances in Water Resources*, vol. 89, pp. 53–66, 2016.
- [2] M. A. Amooie, M. R. Soltanian, and J. Moortgat, "Solutal convection in porous media: Comparison between boundary conditions of constant concentration and constant flux," *Physical Review E*, vol. 98, no. 3, p. 033118, 2018.
- [3] G. M. Homsy, "Viscous fingering in porous media," *Annual review of fluid mechanics*, vol. 19, no. 1, pp. 271–311, 1987.
- [4] M. A. Amooie, M. R. Soltanian, and J. Moortgat, "Hydrothermodynamic mixing of fluids across phases in porous media," *Geophysical Research Letters*, vol. 44, no. 8, pp. 3624–3634, 2017.
- [5] T. Luciani, A. Burks, C. Sugiyama, J. Komperda, and G. E. Marai, "Details-first, show context, overview last: Supporting exploration of viscous fingers in large-scale ensemble simulations," *IEEE Transactions on Visualization and Computer Graphics*, 2018.
- [6] A. Skauge, P. A. Ormehaug, T. Gurholt, B. Vik, I. Bondino, G. Hammon *et al.*, "2-d visualisation of unstable waterflood and polymer flood for displacement of heavy oil," in *Proc. SPE Improved Oil Recovery Symposium*, 2012.
- [7] M. R. Soltanian, M. A. Amooie, Z. Dai, D. Cole, and J. Moortgat, "Critical dynamics of gravito-convective mixing in geological carbon sequestration," *Scientific Reports*, vol. 6, p. 35921, 2016.
- [8] M. A. Amooie, M. R. Soltanian, F. Xiong, Z. Dai, and J. Moortgat, "Mixing and spreading of multiphase fluids in heterogeneous bimodal porous media," *Geomechanics and Geophysics for Geo-Energy and Geo-Resources*, vol. 3, no. 3, pp. 225–244, 2017.
- [9] M. R. Soltanian, M. A. Amooie, N. Gershenzon, Z. Dai, R. Ritz, F. Xiong, D. Cole, and J. Moortgat, "Dissolution trapping of carbon dioxide in heterogeneous aquifers," *Environmental Science & Technology*, vol. 51, no. 13, pp. 7732–7741, 2017.
- [10] X. Fu, L. Cueto-Felgueroso, and R. Juanes, "Pattern formation and coarsening dynamics in three-dimensional convective mixing in porous media," *Phil. Trans. R. Soc. A*, vol. 371, no. 2004, p. 20120355, 2013.
- [11] G. Aldrich, J. Lukasczyk, M. Steptoe, R. Maciejewski, H. Leitte, and B. Hamann, "Viscous fingers: A topological visual analytics approach," *IEEE Scientific Visualization Contest*, vol. 1, no. 2, p. 4, 2016.
- [12] G. Favelier, C. Gueunet, and J. Tierny, "Visualizing ensembles of viscous fingers," in *IEEE Scientific Visualization Contest*, 2016.
- [13] J. Lukasczyk, G. Aldrich, M. Steptoe, G. Favelier, C. Gueunet, J. Tierny, R. Maciejewski, B. Hamann, and H. Leitte, "Viscous fingering: A topological visual analytic approach," in *Applied Mechanics and Materials*, vol. 869, 2017, pp. 9–19.

- [14] C. Steger, "An unbiased detector of curvilinear structures," *IEEE Transactions on Pattern Analysis and Machine Intelligence*, vol. 20, no. 2, pp. 113–125, 1998.
- [15] U. Ayachit, "The paraview guide: a parallel visualization application," 2015.
- [16] H. Childs, E. Brugger, B. Whitlock, J. Meredith, S. Ahern, D. Pugmire, K. Biagas, M. Miller, C. Harrison, G. H. Weber, H. Krishnan, T. Fogal, A. Sanderson, C. Garth, E. W. Bethel, D. Camp, O. Rübel, M. Durant, J. M. Favre, and P. Navrátil, "VisIt: An End-User Tool For Visualizing and Analyzing Very Large Data," in *High Performance Visualization—Enabling Extreme-Scale Scientific Insight*, Oct 2012, pp. 357–372.
- [17] "Tecplot," March 2018, <https://www.tecplot.com/>.
- [18] P. De Anna, M. Dentz, A. Tartakovsky, and T. Le Borgne, "The filamentary structure of mixing fronts and its control on reaction kinetics in porous media flows," *Geophysical Research Letters*, vol. 41, no. 13, pp. 4586–4593, 2014.
- [19] J. Lukasczyk, G. Weber, R. Maciejewski, C. Garth, and H. Leitte, "Nested tracking graphs," *Computer Graphics Forum*, vol. 36, no. 3, pp. 12–22, 2017.
- [20] A. Buka and P. Palffy-Muhoray, "Stability of viscous fingering patterns in liquid crystals," *Physical Review A*, vol. 36, no. 3, p. 1527, 1987.
- [21] A. Buka, P. Palffy-Muhoray, and Z. Racz, "Viscous fingering in liquid crystals," *Physical Review A*, vol. 36, no. 8, p. 3984, 1987.
- [22] E. L. Hinrichsen, K. Maloy, J. Feder, and T. Jossang, "Self-similarity and structure of dila and viscous fingering clusters," *Journal of Physics A: Mathematical and General*, vol. 22, no. 7, p. L271, 1989.
- [23] S. Li, J. S. Lowengrub, J. Fontana, and P. Palffy-Muhoray, "Control of viscous fingering patterns in a radial hele-shaw cell," *Physical review letters*, vol. 102, no. 17, p. 174501, 2009.
- [24] M. de Saint-Venant, "Surfaces à plus grande pente constituées sur des lignes courbes," *Bulletin de la Société Philomathématique de Paris*, pp. 24–30, 1852.
- [25] T. Lindeberg, "Edge detection and ridge detection with automatic scale selection," *International Journal of Computer Vision*, vol. 30, no. 2, pp. 117–156, 1998.
- [26] J. D. Furst and S. M. Pizer, "Marching ridges," in *SIP*, 2001, pp. 22–26.
- [27] R. Peikert and F. Sadlo, "Height ridge computation and filtering for visualization," in *Proc. IEEE Pacific Symposium on Visualization*, 2008, pp. 119–126.
- [28] N. D. Cornea, D. Silver, and P. Min, "Curve-skeleton properties, applications, and algorithms," *IEEE Transactions on Visualization and Computer Graphics*, vol. 13, no. 3, pp. 0530–548, 2007.
- [29] S. Biasotti, D. Giorgi, M. Spagnuolo, and B. Falcidieno, "Reeb graphs for shape analysis and applications," *Theoretical Computer Science*, vol. 392, no. 1-3, pp. 5–22, 2008.
- [30] F. Lazarus and A. Verroust, "Level set diagrams of polyhedral objects," in *Proc. ACM Symposium on Solid Modeling and Applications*, 1999, pp. 130–140.
- [31] M. Van Kreveld, R. van Oostrum, C. Bajaj, V. Pascucci, and D. Schikore, "Contour trees and small seed sets for isosurface traversal," in *Proc. Annual Symposium on Computational Geometry*, 1997, pp. 212–220.
- [32] J. Tierny, G. Favelier, J. A. Levine, C. Gueunet, and M. Michaux, "The topology toolkit," *IEEE Transactions on Visualization and Computer Graphics*, vol. 24, no. 1, pp. 832–842, 2018.
- [33] C. Gueunet, P. Fortin, J. Jomier, and J. Tierny, "Task-based Augmented Reeb Graphs with Dynamic ST-Trees," in *Proc. Eurographics Symposium on Parallel Graphics and Visualization*, H. Childs and S. Frey, Eds. The Eurographics Association, 2019.
- [34] J. Damon, "Properties of ridges and cores for two-dimensional images," *Journal of Mathematical Imaging and Vision*, vol. 10, no. 2, pp. 163–174, 1999.
- [35] D. Eberly, *Ridges in image and data analysis*. Springer Science & Business Media, 2012, vol. 7.
- [36] L. Vincent and P. Soille, "Watersheds in digital spaces: an efficient algorithm based on immersion simulations," *IEEE Transactions on Pattern Analysis & Machine Intelligence*, no. 6, pp. 583–598, 1991.
- [37] C. Heine, D. Schneider, H. Carr, and G. Scheuermann, "Drawing contour trees in the plane," *IEEE Transactions on Visualization and Computer Graphics*, vol. 17, no. 11, pp. 1599–1611, 2011.
- [38] H. Doraiswamy and V. Natarajan, "Output-sensitive construction of reeb graphs," *IEEE transactions on visualization and computer graphics*, vol. 18, no. 1, pp. 146–159, 2012.
- [39] U. Bauer, X. Ge, and Y. Wang, "Measuring distance between reeb graphs," in *Proc. Annual Symposium on Computational Geometry*, 2014, p. 464.
- [40] H. Carr, J. Snoeyink, and M. van de Panne, "Flexible isosurfaces: Simplifying and displaying scalar topology using the contour tree," *Computational Geometry*, vol. 43, no. 1, pp. 42–58, 2010.
- [41] D. Silver and X. Wang, "Volume tracking," in *Proc. Visualization*, 1996, pp. 157–ff.
- [42] M. Balzer and O. Deussen, "Voronoi treemaps," in *Proc. IEEE Symposium on Information Visualization*, 2005, pp. 49–56.
- [43] J. Marino and A. Kaufman, "Planar visualization of treelike structures," *IEEE Transactions on Visualization and Computer Graphics*, vol. 22, no. 1, pp. 906–915, 2016.
- [44] B. Johnson and B. Shneiderman, "Tree-maps: A space-filling approach to the visualization of hierarchical information structures," in *Proc. Visualization*, 1991, pp. 284–291.
- [45] J. Wood and J. Dykes, "Spatially ordered treemaps," *IEEE Transactions on Visualization and Computer Graphics*, vol. 14, no. 6, 2008.
- [46] M. Bruls, K. Huizing, and J. J. Van Wijk, "Squarified treemaps," in *Data visualization*, 2000, pp. 33–42.
- [47] C. A. Brewer, "Colorbrewer: Color advice for maps," September 2018, <http://www.ColorBrewer.org>.
- [48] O. A. Çakiroğlu, C. Erten, Ö. Karataş, and M. Sözdinler, "Crossing minimization in weighted bipartite graphs," in *International Workshop on Experimental and Efficient Algorithms*, 2007, pp. 122–135.
- [49] A. Yamaguchi and A. Sugimoto, "An approximation algorithm for the two-layered graph drawing problem," in *International Computing and Combinatorics Conference*, 1999, pp. 81–91.
- [50] K. Sugiyama, S. Tagawa, and M. Toda, "Methods for visual understanding of hierarchical system structures," *IEEE Transactions on Systems, Man, and Cybernetics*, vol. 11, no. 2, pp. 109–125, 1981.
- [51] R. M. Haralick, "Ridges and valleys on digital images," *Computer Vision, Graphics, and Image Processing*, vol. 22, no. 1, pp. 28–38, 1983.



Jiayi Xu is a Ph.D. student in Computer Science and Engineering at the Ohio State University. He received his B.E. degree with Chu Kochen Honors from the College of Computer Science and Technology at Zhejiang University in 2014. His research interests include graph visualization and scientific feature tracking.



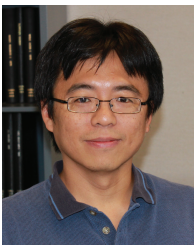
Soumya Dutta is a staff scientist in Data Science at Scale team at Los Alamos National Laboratory. He received his B.Tech. degree in Electronics and Communication Engineering from West Bengal University of Technology in August 2009, and M.S. and the Ph.D. degree in Computer Science and Engineering from the Ohio State University in May 2017 and May 2018 respectively. His research interests are statistical data summarization and analysis; in situ data analysis, reduction, and feature exploration; uncertainty analysis; and time-varying, multivariate data exploration.



Wenbin He is a Ph.D. student in computer science and engineering at the Ohio State University. He received his B.S. degree from the Department of Software Engineering at Beijing Institute of Technology in 2012. His research interests include visualization and analysis of large-scale scientific data, uncertainty visualization, and flow visualization.



Joachim Moortgat is an Associate Professor in the School of Earth Sciences, Ohio State University. Moortgat holds MS degrees in theoretical physics and astrophysics, both from Utrecht University, and a PhD in astrophysics from the Radboud University, The Netherlands. Moortgat was the recipient of the 2014 SPE Cedric K. Ferguson Medal awarded by the Society of Petroleum Engineers. His research interests lie in the theory and advanced numerical modeling of compositional multiphase flow in subsurface fractured porous media.



Han-Wei Shen is a full professor at the Ohio State University. He received his B.S. degree from Department of Computer Science and Information Engineering at National Taiwan University in 1988, the M.S. degree in computer science from the State University of New York at Stony Brook in 1992, and the Ph.D. degree in computer science from the University of Utah in 1998. From 1996 to 1999, he was a research scientist at NASA Ames Research Center in Mountain View California. His primary research

interests are scientific visualization and computer graphics. He is a winner of the National Science Foundations CAREER award and U.S. Department of Energys Early Career Principal Investigator Award. He also won the Outstanding Teaching award twice in the Department of Computer Science and Engineering at the Ohio State University.